ABSTRACT BOOK

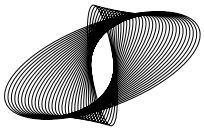

3rd MR IN RT SYMPOSIUM

16–17 June 2015 | Lund, Sweden

CONTENT

Day 1

Day 2

Poster viewing

DAY 1, 11:00–11:15

CORRECTION OF GEOMETRIC DISTORTIONS AND SIGNAL PILE-UP IN DIFFUSION WEIGHTED ECHO-PLANAR IMAGES

L.D. van Buuren, D. Polders, M. Milder, U.A. van der Heide
Netherlands Cancer Institute

Introduction: Diffusion MRI is used in RT to improve tumor delineation and monitor treatment response. To minimize scan time, echo-planar imaging (EPI) is employed. The low pixel bandwidth in the phase-encoding (PE) direction of EPI causes geometric distortions due to variations in the main magnetic field (B0). This results in shifts, compression or stretching and associated intensity changes within the image. Previously, methods have been developed to correct for distortions based on a measured B0 map or by combining EPI images obtained with opposite gradients (see ref. 1). However, for severe changes in B0, occurring in close vicinity of gas pockets in the rectum or in the head and neck region, the corrections fail. Here signal pile-up occurs, for which signals from non-neighboring voxels are acquired in the same EPI location. We demonstrate that EPI images can be corrected even for signal pile-up using a combination of the above mentioned methods.

Methods: We scanned a phantom consisting of six water tubes positioned around a central tube filled with air, and emerged in ice water. The phantom was scanned using opposite PE gradients with a pixel band widths ranging from 15 to 44 Hz in the PE direction, comparable to clinical protocols. Additionally, we acquired dual gradient echo sequences to map the B0 field.

Our correction method, which employs a reversed gradient EPI image in addition to the B0 map to recover the information loss in regions with signal pile-up, was compared to raw EPI images and the standard B0 correction method. Its effect was measured by the change in signal homogeneity in the tube with largest signal pile-up, quantified by the coefficient of variation (CoV), defined as the ratio of the standard deviation and the signal mean.

Results: Large distortions (~1cm) of the tubes and variations in intensities were visible in the uncorrected EPI images. In addition, we observed signal pile-up and signal loss in regions with large B0 gradients in PE direction. With the B0 based correction method, distortions of the tubes and intensity variations within the tubes were removed, but pile-up and signal loss were still visible. These were strongly reduced in our method, where we added information from the image with a reversed gradient. This was confirmed by the change in CoV. The coefficient was 0.34 and 0.35 for the raw EPI image and B0 corrected image, respectively and decreased to 0.14 after applying the proposed correction method.

Conclusions: Our method has shown improvements in the correction of EPI images. It corrects not only for the compression and stretching within the images, but also for the information loss, which can occur near gas pockets. This principle allows constructing an undistorted ADC map, which can be used for tumor delineation and response monitoring.

Ref 1: Jezzard, P., Correction of geometric distortion in fMRI data.,
NeuroImage 62 (2012), 648–651

DAY 1, 11:15–11:30

FEASIBILITY OF SELF-NAVIGATED PHASE-RESOLVED 4D MRI USING GOLDEN ANGLE RADIAL

Eric Paulson, Nikolai Mickevicius, Habib Al saleh
Radiation Oncology, Radiology, Biophysics, Medical College of Wisconsin, Milwaukee, Wisconsin, United States

Purpose: Knowledge of tumor and organ at risk motion trajectories is critical in radiation therapy and is one of the driving factors behind MRI-gRT. However, acquisition of true 4D-MR images is challenged by spatial, temporal, and contrast resolution demands. The goal of this work was to explore the feasibility of using the self-navigating properties of radial k-space trajectories to guide the reconstruction of phase-resolved 4D-MR images.

Methods: Images were acquired in healthy volunteers on a Siemens 3T scanner using a hybrid 3D radial sequence of our own design with switchable SPGR and bSSFP contrast modes. The sequence utilized Cartesian sampling with volumetric interpolation along the partition direction and in-plane golden angle radial sampling. Slab-selective, axial images were acquired continuously for about six minutes. All partitions were acquired before the spoke angle was incremented. Following acquisition, the raw k-space data were transferred to a remote workstation. Gradient group delays were corrected using an iterative approach. The respiratory waveform was extracted by projecting the center of each spoke of each partition for a given spoke angle along kz, performing a 1D FFT, and calculating a signal-weighted center of mass. The respiratory waveform was smoothed and peaks corresponding to inspiration were auto-detected. Time intervals between the start of each respiratory phase cycle were calculated and decimated into ten-phase bins. A lookup table of bin indices was generated and used to reshuffle the 3D+time k-space data (corrected for group delays), k-space trajectory, and density compensation waveform. Following reshuffling, images were reconstructed for each of the ten phase bins by applying a 1D FFT along kz and NUFFTs along kx-ky.

Results: Respiratory waveforms were extractable for both SGPR and bSSFP acquisitions. However, the waveforms were found to vary based on anatomy-coil proximity, indicating that coil combination may mask or alter respiratory waveforms. Deep breath holds performed by one volunteer were clearly discernable in the extracted respiratory waveforms, with no signal saturation detected. Compared to original images, the phase-resolved 4D-MR images demonstrated substantial improvement in image sharpness over each of the ten respiratory phase bins.

Discussion: Acquisition of phase-resolved 4D MR images using self-navigated radial trajectories is feasible. Radial k-space trajectories ensure the center of k-space is covered following reshuffling, which eliminates shading artifacts in the phase-resolved 4D MR images. In addition, the repeated covering of the center of k-space provides the time-efficient self-navigation properties that eliminates: 1) the need for external respiratory or image-based surrogates, 2) asynchronous phase shifts between surrogate and image acquisitions, 3) saturation or gain resetting of surrogate signals. Since each golden angle radial spoke is acquired at a unique angle (111.246 deg), all acquired data can be utilized during reconstruction of phase-resolved 4D MR images (as opposed to using a linear combination of repeated k-space locations). Finally, the flexibility provided by switchable SPGR or bSSFP contrast modes may be advantageous for disease sites that benefit more from T1 versus mixed T2/T1 contrast.

DAY 1, 11:30–11:45

CLINICAL IMPLEMENTATION OF MRI-ONLY FOCAL BRAIN SIMULATION

James Balter, Yue Cao, Shu-Hui Hsu, Eric Paradis, Lianli Liu, Xiaoping Chen, Jim Irrer, Mary Feng, Theodore Lawrence
The University of Michigan

Introduction: As part of an overall plan to integrate MRI into routine clinical operation, a series of projects was initiated to support the use of MRI without CT in the routine clinical workflow for external beam radiotherapy. This report describes our current state of MRI-only simulation for treatment of intracranial targets.

Methods: In order to support routine clinical use of our 3 T MRI scanner (Skyra, Siemens, Germany) without CT in the head, a series of steps were followed. First, system-level distortion was measured using a custom-built large volume grid phantom. Next, a method for generating synthetic CT ("MRCT") image volumes from MRI scans was developed and optimized for robust use. Both scanning techniques as well as post-processing methods were iteratively improved and tested by scanning 16 patients with MRI and CT under an institution-approved protocol. An automated software tool was developed to generate MRCT images by sending component MR images to a DICOM node. Parallel efforts were applied to estimate the magnitude of, and develop methods to correct, subject-induced distortions. An initial release of MRI-only whole brain simulation in 2013 was predicated on demonstrating equivalent clinical decisions (monitor units and DRR similarity). To support focal brain radiotherapy, an optimized set of scans (volumetric T1-weighted Dixon, T2, Ultrashort TE (PETRA) and time-of-flight) and post-processing techniques (including air and vessel masking, bias field correction and intensity normalization, fuzzy c-means classification and probabilistic integration of assigned densities) were developed and resulting MRCT image volumes were tested for equivalence in meeting clinical treatment planning directives for volumetric modulated arc therapy (VMAT).

Results: System-level distortions were determined to be sub-mm over the space spanned by the head, and thus no further correction for these effects was warranted. Subject-specific susceptibility effects have the potential to lead to distortions of up to 3 mm at the inferior frontal lobe for lower bandwidth clinical scans (e.g. T1-MPRAGE) without patient-specific distortion correction, which is pending. No significant differences were found between CT and MRCT plans in total MU delivered (-0.4% mean), PTV D95% (-0.2% mean, range -0.1 to -0.6%), PTV D5%(0.0% mean, range -0.4 to 0.3%), PTV Dmax (-0.3% mean, range -0.9 to -0.1%), or Dmax values for OARs that approached the plan limits set for optimization. Gamma analysis showed no significant differences between doses calculated using the same VMAT fluences on density grids from MRCT versus corresponding CT image volumes. Following release of an FDA-cleared version of the PETRA sequence, two patients were simulated with MRI and a CT backup for workflow optimization and final clinical checks.

Summary: A detailed process for optimizing, evaluating, and clinically implementing MRI-only simulation for focal brain radiotherapy has been completed. MRI is now permitted for use without CT in support of focal brain radiotherapy in our department. Subject-specific distortion analysis and correction is being tested for clinical release. Future projects will include releases of MRI-only simulation for external beam radiotherapy in the abdomen, pelvis and neck.

Supported by NIHR01EB016079 and Siemens Medical Systems

DAY 1, 11:45–12:00

PATIENT INDUCED SUSCEPTIBILITY EFFECTS*

Josef Lundman, Mikael Bylund, Anders Garpebring, Tufve Nyholm
Umeå University

Introduction: Magnetic resonance imaging (MRI) is increasing in use in radiotherapy. It has been shown to be superior to CT for target delineation due to soft tissue contrast. With MRI, there is also the possibility for functional imaging using diffusion weighted and contrast enhanced imaging. Compared to X-ray based image acquisition, the MRI is, however, more complex and this results in uncertainties in the geometrical representation of the imaged volume. In modern MR systems, where the homogeneity of the main magnetic field is very high, gradient field non-linearities are often the dominating source of such distortions. These distortions can be corrected for with good result using distortion correction algorithms provided by all major vendors. The patient itself also introduces variations in the main magnetic field. These variations can in turn lead to distortions which are not possible to correct for with existing distortion correction algorithms. Neither can they be measured using a phantom and they are difficult to quantify for the individual patient. Increasing the bandwidth can reduce these distortions at the cost of a reduced signal to noise ratio. The goal of the current work was to develop a method for simulation of the introduced variation in the magnetic field caused by the patient, for different sites in the body. The goal was to objectively identify a balanced acquisition bandwidth for different anatomical regions, so that the patient induced susceptibility distortions stay within acceptable limits.

Method: Patient induced MRI susceptibility effects were simulated in whole-body CT acquisitions. Each pixel in the CT images were assigned susceptibilities based on CT number. In this assignment, susceptibility values were specified for four materials/tissues at specific HU, air (0.36E-6, -1000 HU), fat (-7.79E-6, -120 HU), muscle (-9.00E-6, 100 HU) and bone (-11.31E-6, 700 HU). Between the set HU-values the susceptibility assignment was interpolated. Every pixel with a value below -1000 HU or above 700 HU was assigned the susceptibility of air and bone, respectively. From this set of assigned susceptibilities, matrices of the local magnetic field in each pixel was calculated using a first order approximation. Images containing patient induced susceptibility effects were then calculated using these matrices.

Results: The local B0 field resulting from the susceptibility of the patient tissues was simulated for whole body CT acquisitions. In the lung region the distortion of the local magnetic field varied in an interval of approximately -8 ppm to 4 ppm, for a 1.5 T field. The corresponding interval for a simulated 3 T field was approximately -16 ppm to 7 ppm.

Conclusion: The method used provides an easy way of obtaining a simulation of the patient induced MRI susceptibility effects from an anatomical image. This can in turn be used to identify balanced acquisition bandwidths for MRI acquisitions or to estimate the distortions in different anatomical regions in an objective way.

DAY 1, 14:40–14:55

PRELIMINARY RESULTS SUPPORTING AN MRI-ALONE WORKFLOW FOR EXTERNAL BEAM PROSTATE RADIOTHERAPY

Dowling J.A.[1], Pichler P.[2], Sun J.[3], Rivest-Henault D.[1], Ghose S.[1], Martin J.[2], Wratten C.[2], Arm, J. [4], Fripp J.[1], Greer P.B.[2]

(1) Commonwealth Scientific and Industrial Research Organisation Australian E-Health Research Centre Brisbane Australia
(2) Calvary Mater Newcastle Hospital Radiation Oncology Newcastle Australia
(3) University of Newcastle Hospital Radiation Oncology Newcastle Australia
(4) Department of Radiology, Hunter New England Health, Calvary Mater Newcastle, NSW, Australia.

Introduction: We describe methods to accurately generate substitute CT (sCT) scans from standard MR pelvic scans for MR-Sim prostate treatment planning.

Material/methods: A Siemens Skyra 3T MR scanner with laser bridge, flat couch top and pelvic coil mounts was used to scan 39 patients scheduled for external beam radiation therapy for localized prostate cancer. The scan used for sCT generation were a 1.6 mm 3D isotropic T2w (SPACE). Three additional scans prostate scans were acquired: a T2w, a T2*w and a T1w flip angle 80^0 for gold fiducials. Within two hours of MR scanning each patient also received a routine planning CT scan. Manual contouring of the rectum, bladder and pelvic bones was performed independently on the CT and whole pelvis MR scans. The prostate was contoured on the small field of view T2w scan. Three experienced observers contoured each organ on MRI allowing inter-observer quantification. To generate a training database, each patient CT scan was co-registered to their whole pelvis T2w using symmetric rigid registration followed by structure guided deformable registration to maintain bone rigidity while allowing high quality bladder and rectum registration. A local weighted voting method was used to generate sCT and automatic contouring results. This involved four main steps: First pairwise registration of each whole pelvis MRI in the training database (and associated contours) to the target MRI (rigid followed by diffeomorphic demons registration). Secondly a patch around each voxel in the target MRI was compared with patches in the same geographical location on the registered MRI images and a similarity computed (sum of squared differences). Third, this similarity was then used as a weighting to generate the estimated HU from the co-registered CT's. Finally the same similarity was used to determine the spatial locations for each contour and automatic contours generated. The generated sCT and structures were automatically converted to a DICOM-RT directory.

Results: The mean error in Hounsfield units (HU) between the sCT and actual patient CT data (within the body contour) was 0.6±14.7 (mean ± 1 SD). The mean absolute error (MAE) within the body contour was 40.5±8.2 HU. The Dice similarity coefficient (DSC) results for inter-observer contouring differences (n=20, 3 observers, planning MRI) were: prostate 0.85 ± 0.09, bladder 0.95 ± 001 and rectum 0.84 ± 0.07. Automatic organ contouring results generated and compared to manual contours for the full 39 patient datasets were close to the inter-observer level: prostate 0.80 ± 0.08, bladder 0.86 ± 0.12, rectum 0.84 ± 0.06, bones: 0.91 ± 0.03 and body:1.00 ± 0.003. With 2Gy prescribed doses at the International Commission on Radiation Units (ICRU) point, the change in monitor units (MU) between the sCT-based plans relative to that of the gold standard CT plan was found to be 0.3 ± 0.8%.

Conclusions: We have significantly improved the accuracy of sCT generated from MR compared to previous techniques. Our sCT generation method utilizes standard MR sequences. A prospective trial of MR-alone planning using the sCT method will commence in 2015.

DAY 1, 14:55–15:10

ACCURATE MRI ONLY PROSTATE RADIOTHERAPY PLANNING USING THE STATISTICAL DECOMPOSITION ALGORITHM

Carl Siversson[1,2], Fredrik Nordström[2, 3, 4], Terese Nilsson[2], Tufve Nyholm[5], Joakim Jonsson[5], Adalsteinn Gunnlaugsson[6], Lars E. Olsson[1]

(1) Department of Medical Radiation Physics, Lund University, Malmö, Sweden
(2) Spectronic Medical AB, Helsingborg, Sweden
(3) Department of Radiation Physics, Skåne University Hospital, Lund, Sweden
(4) Department of Medical Radiation Physics, Lund University, Lund, Sweden
(5) Department of Radiation Sciences, Umeå University, Umeå, Sweden
(6) Department of Oncology, Skåne University Hospital, Lund University, Lund, Sweden

Introduction/purpose: In order to enable an MRI-only workflow in radiotherapy treatment planning, methods are required for generating Hounsfield unit maps (i.e. synthetic CT, sCT) for dose calculations, directly from MRI. The Statistical Decomposition Algorithm (SDA) is a method for automatically generating such sCT images from a single MR image volume. The SDA automatically decomposes an MRI into a plurality of tissue types, which are then statistically analyzed to reconstruct the most probable CT representation for each tissue type, based on a multi-template material consisting of both MRI and CT. The aim of this pilot study is to evaluate sCT images generated by the SDA for input to dose calculations, by comparing dosimetric accuracy between sCT and conventional CT for a set of prostate cancer patients. We also evaluate the effect of variation in patient geometry between CT and MRI imaging sessions.

Methods/materials: The study comprised six prostate cancer patients, for whom a three-dimensional T2 weighted MRI and a conventional planning CT were acquired. Volume coverage was similar between the images. For each patient, sCT images were generated from the acquired MRI using the SDA. In order to decouple the effect of variations in patient geometry between imaging modalities from the effect of uncertainties in the SDA, the conventional CT was non-rigidly registered to the MRI to assure that their geometries were perfectly aligned. For each patient, a 6 MV volumetric modulated arc therapy (VMAT) plan was created for the registered CT (rCT), and recalculated for both the sCT and the conventional CT. The dose distributions for each type of attenuation map were evaluated using several methods, including a set of dose-volume histogram parameters and a restrictive gamma criterion (2% local dose/1mm with superficial points excluded).

Results: Average mean absorbed dose difference to target was 0.0±0.2% (1 s.d.) between sCT and rCT, whereas it was -0.1±0.2% (1 s.d.) between CT and rCT. Average absorbed dose differences between sCT and rCT were -0.2±0.3%, 0.0±0.3% and -0.1±0.4% (1 s.d.), for bladder, rectum and femoral heads respectively. Corresponding values between CT and rCT were 0.8±1.9%, 1.0±0.8% and -0.1±2.0% (1 s.d.). The average gamma pass rate was 100% for sCT vs. rCT, whereas it was 90.2% for CT vs. rCT.

Conclusions/discussion: The dosimetric uncertainties originating from the sCT images are notably lower than the uncertainties introduced by variations in patient geometry between imaging sessions. These variations are assumed to primarily originate from uncertainties in patient repositioning between MRI and CT. However, such conclusion assumes that geometry distortions in the MRI are small, which should be the case given the measures taken (i.e. high bandwidth and distortion correction). The literature suggests that an overall dose accuracy of 2.5-3.5% is needed to meet the clinical requirements concerning high tumor control probability and minimal risk to normal tissue. Thus, it appears that the uncertainty contribution added by the SDA is nearly negligible in this context and that a highly accurate MRI only workflow in prostate radiotherapy planning is feasible using the SDA.

DAY 1, 15:10–15:25

EVALUATION OF METHODS FOR TUMOR SEGMENTATION ON DIFFUSION WEIGHTED MRI FOR TREATMENT RESPONSE ASSESSMENT DURING RADIOTHERAPY OF LOCALLY ADVANCED CERVICAL CANCER

Søren Haack[1,2], Kari Tanderup[2], Jesper Folsted Kallehauge[3], Sandy Mohamed Ismail Mohamed[2,4], Jacob Christian Lindegaard[2], Erik Morre Pedersen[5], Sune Nørhøj Jespersen[6,7]

(1) Department of Clinical Engineering, Aarhus University Hospital, Aarhus Denmark
(2) Departmant of Oncology, Aarhus University Hospital, Aarhus Denmark
(3) Department of Medical Physics, Aarhus University Hospital, Aarhus Denmark
(4) Department of Radiotherapy, National Cancer Institute, Cairo University, Egypt
(5) Department of Radiology, Aarhus University Hospital, Aarhus Denmark
(6) CFIN/MindLab, Aarhus University, Aarhus, Denmark
(7) Department of Physics and Astronomy, Aarhus University, Aarhus, Denmark

Introduction: Diffusion weighted MRI (DW-MRI) and the derived Apparent Diffusion Coefficient (ADC) value has potential value for monitoring tumor response to radiotherapy (RT). However, the method used for segmentation of volumes with reduced diffusion will influence both the size of the volume as well the observed distribution of ADC values. This study evaluates 1) different segmentation methods, and 2) how they affect assessment of tumor ADCs during RT.

Materials and methods: Eleven patients with locally advanced cervical cancer underwent MRI examination three times during their RT: prior to start of RT (PRERT), two weeks into external beam RT (WK2RT) and one week prior to brachytherapy (PREBT). Volumes on DW-MR images were segmented using three semi-automatic segmentation methods: "cluster analysis", "relative signal intensity" (SD4) and "region growing". Segmented volumes were compared to the gross tumor volume (GTV) identified on T2 weighted MR images using the Jaccard Similarity Index (JSI). ADC values from segmented volumes were compared and changes of ADC during therapy were evaluated.

Results: A significant difference between the four volumes (GTV, DWIcluster, DWISD4 and DWIregion) was found ($p < 0.01$), and the volumes changed significantly during treatment ($p < 0.01$). There was a significant difference in JSI among segmentation methods at time of PRE-RT ($p < 0.016$), with cluster analysis and relative signal intensity having the highest JSI (0.52 and 0.50), and region growing having the lowest JSI (0.35). There was no significant difference in mean ADC when comparing the ADC values of tumor volume between the three different segmentation methods at same treatment time, but the mean tumor ADC increased significantly ($p < 0.01$) for all methods when compared across treatment time. Using the relative signal intensity method the kurtosis of ADC histogram analysis decreased significantly during treatment and a significant correlation ($r = -0.83$, $p < 0.002$) was found between changes in ADC from PRERT to WK2RT compared to ADC at PRERT.

Conclusion: The volume size of segmented tumor with hyper-intense intensities on DW-MR images depends significantly of segmentation Among the 3 semi-automatic segmentations of hyper-intense intensities on DW-MR images implemented, cluster analysis and relative signal thresholding had the greatest similarity to the clinical tumor volume. Evaluation of mean ADC was robust and did not depend on segmentation method. Evaluation of mean ADC was robust and did not depend on segmentation method.

DAY 1, 15:25–15:40

VALIDATION OF MR-BASED DENSITY MAPS FOR RADIATION TREATMENT PLANNING OF THE PELVIS

Steffen Renisch[1], Heinrich Schulz[1], Max Köhler[2], Michael Helle[1], Marloes Frantzen-Steneker[3], Uulke van der Heide[3]

(1) Philips Research Laboratories, Hamburg, Germany
(2) Philips Healthcare, MR Therapy, Vantaa, Finland
(3) Department of Radiotherapy, Antoni van Leeuwenhoek, Amsterdam, The Netherlands

Purpose: One of the crucial components in the design of an external beam radiation treatment workflow based on MR imaging is the generation of density maps from MR images for the treatment simulation. We designed an algorithm (Magnetic Resonance for Calculating Attenuation, "MRCAT") providing those density maps based on an easy to use and fast mDixon sequence. Here the analysis and validation of those maps is shown.

Methods/Materials: For this study, 20 patients with an indication of prostate EBRT received an additional mDixon scan (Philips Achieva TX 3T, 3D Cartesian FFE acquisition, TE1/TE2 = 1.1ms/2.1ms, TR = 3.3ms, = 10°, 1.7x1.7x2.5mm3 acquired voxel size, 300x400x350 mm3 FOV, 1:49min imaging time). Subsequently those patients underwent the standard CT-based treatment planning workflow; in addition the MRCAT images were computed, and the treatment simulation was repeated on the MRCAT images. In addition, volunteer images were acquired on Philips Ingenia 1.5T (TE1/TE2 = 1.6ms/3.7ms, TR = 5.6ms) and 3T (TE1/TE2 = 1.2ms/2.3ms, TR = 3.9ms) scanners otherwise using the same protocol. One crucial step in the MRCAT generation is the segmentation of the body outline and of the bone structures. This step was validated using manual ground-truth annotations on the Ingenia data. For a validation of the HU value assignment, the average HU values are correlated between the MRCAT maps and the actual CT images. Finally, the dose distributions resulting from the simulation based on the CT images are compared with the respective dose distributions when using MRCAT images as density maps. For this comparison a gamma analysis is used.

Results: For the validation of the segmentation, the bone structures were assessed individually. For the femur bones an average segmentation error below 1mm was found. The average segmentation error of the pelvis bones was below 1.3mm, with an average 95% quantile still below 2mm. The most challenging structure was the sacrum with an average segmentation error slightly above 2mm, which is still very good given the voxel size. Looking at the HU values, the correlation between the average HU values of the CT images and those of the MRCAT images is very good with a correlation coefficient of 0.953. A linear regression reveals a slight underestimation of the HU values on the MRCAT images of about 5HU. Finally, a 3%/3mm gamma analysis of the 75% isodose region of the MRCAT-based dosimetry compared to CT-based dosimetry shows that on average 99.98% of the voxels have a gamma < 1, i.e. the dose distributions are sufficiently close to fulfil the criterion. The average gamma is 0.26 (stdev 0.04), the average 99% quantile is 0.55 (stdev 0.09). Isocenter doses are overestimated on average by 1.4±0.2%.

Discussion and Conclusion: The segmentation results show that the segmentation as a core component of the MRCAT algorithm is working accurately and robustly. No coarse errors were observed on the study data. Both the density comparison and the gamma analysis indicate that the dosimetry using MRCAT maps are sufficiently close to CT-based dosimetry to be applicable in clinical practice.

DAY 1, 15:40–15:55

VALIDATION OF K-T T2 MAPPING FOR TREATMENT RESPONSE MONITORING*

Petra J van Houdt[1], Harsh K Agarwal[2], Laurens D van Buuren[1], Marko Ivancevic[3], Ghazaleh Ghobadi[1], Floris Pos[1], Uulke A van der Heide[1]

(1) Department of Radiation Oncology, the Netherlands Cancer Institute, Amsterdam, The Netherlands
(2) Philips Research NA, Briarcliff manor, NY, USA
(3) Philips Healthcare, Best, The Netherlands

Introduction: T2 is a potential biomarker for radiotherapy response monitoring of patients with prostate cancer. Recently an accelerated multi-echo spin-echo T2 mapping technique (k-t T2) has been validated for whole-prostate imaging in a clinically reasonable time [1,2]. A key requirement for use of this technique in longitudinal studies is good reproducibility over multiple visits. Therefore, the purpose of this study was to establish the reproducibility of T2 maps using k-t T2 technique.

Methods: To test the stability of the k-t T2 sequence itself, phantom measurements were performed on two clinical MR platforms (1.5T and 3T Achieva, Philips, the Netherlands). We optimized the k-t T2 sequence for each platform to account for differences in scanner hardware (FOV 170x170x170 mm3; voxel size 1.5x1.5x3 for 1.5T vs. 0.8x0.8x3 mm3 for 3T; TR/TE 2693/11 vs. 2459/16 ms; no. of echoes 16 vs. 11; partial-Fourier factor 0.625; SENSE factor 2; k-t T2 reduction factor 4). The Eurospin T05 phantom was used with gel samples of varying T2 values (range 49-212ms; Diagnostic Sonar, Livingston, Scotland). Measurements were repeated monthly for nine months. T2 values were estimated per tube and compared to the average T2 values across measurements to determine the relative difference. The long-term variation is expressed as the average standard deviation of the relative differences. To test clinical reproducibility nine patients with prostate cancer underwent a multi-parametric MRI (3T) prior to surgery. Average time interval between two scan sessions was three weeks. The transversal T2w MRI of the second scan session was rigidly registered to the MRI of the first session. The same transformation was applied to the T2 map. The prostate, normal peripheral zone (PZ), normal central gland (CG), and suspected tumor tissue regions were delineated. We excluded hemorrhage areas visible on T1w from all delineations. The relative difference between the average T2 values in the prostate was determined across all patients. In addition, mean and standard deviation of T2 values per region were determined.

Results: Long-term phantom measurements showed variations in T2 values of 0.9% for 1.5T and 1.1% for 3T. The relative difference in T2 values for the whole prostate gland was 3.2±4.5% across all patients. The average mean T2 value of suspected tumor tissue was 80.0±4.5ms, whereas T2 of normal PZ and CG was 117.6±14.7ms and 98.2±10.4ms, respectively. Heterogeneity inside each ROI is represented by the average standard deviation across all patients: 13.2ms for tumor tissue, 42.6ms for PZ, and 33.8ms for CG.
Discussion and Conclusion:The day-to-day variations of the k-t T2 sequence are small compared to the difference in T2 values for tumor and normal PZ. The differences for patients are on average larger than for phantom data due to lower signal-to-noise, different coil loading, and motion. Further voxel-based repeatability analyses of the data are required to estimate the detectable difference in T2 values that can be attributed to a treatment effect.

References

[1] Liu et al. Magn Reson Med 2011; [2] Agarwal et al. ISMRM 2013 1373.

Acknowledgements DR THERAPAT (FP7-ICT-2011-9, Project 600852).

DAY 1, 15:55–16:10

ADVANTAGES OF RADIAL CAIPI FOR REAL-TIME MOTION MANAGEMENT IN MRI-GRT

Nikolai J. Mickevicius, Eric S. Paulson
Radiation Oncology, Radiology, Biophysics, Medical College of Wisconsin, Milwaukee, Wisconsin, United States

Purpose: Exception gating and dynamic MLC tracking on MRI-gRT systems require extremely low latencies in the image acquisition, reconstruction, and segmentation chain. Multi-band excitation is an emerging MRI acceleration technique that simultaneously excites a short comb of 2D slices, thereby increasing effective temporal resolution by accelerating acquisition in the slice-select direction. However, separation of aliased slices acquired with multi-band Cartesian trajectories requires differences in coil sensitivities and use of SENSE or slice-GRAPPA reconstruction techniques. Alternative RF coil designs and configurations employed in many MRI-gRT systems may challenge the former, while the latter may increase reconstruction latencies to a point that prohibits use in exception gating and dynamic MLC tracking. To this end, we demonstrate here the advantages of radial CAIPIRINHA (CAIPI) for MRI-gRT.

Methods: Custom multi-band, phase-controlled Shinnar-Le Roux RF pulses were designed and implemented into a golden angle radial sequence of our own design with switchable SPGR and bSSFP contrast modes. The phase of the RF pulses was cycled with acquisition of each spoke according to a schedule based on the number of simultaneously excited slices (e.g [0,pi/2; 0,–pi/2; …] for dual-band excitation). Time series of dynamic radial CAIPI images were acquired on an MRI-compatible motion phantom (CIRS), and in healthy volunteers and patients on a Siemens 3T Verio. Following acquisition, the raw k-space data were transferred to a remote workstation for reconstruction in Matlab. Separation of aliased slices was performed by adding the conjugate phase of the RF phase cycling pattern applied to the particular slice of interest. Gradient group delays were corrected using an iterative approach. Images of the separated slices were then reconstructed using the NUFFT.

Results: SAR limited the multi-band RF pulse flip angles to 50 degrees for bSSFP radial CAIPI acquisitions at 3T. Due to the use of conjugate phase, separation of aliased slices required no additional reconstruction overhead. Robust tri-band (i.e., 3 simultaneously excited slices) images were acquired at 9 frames/sec. Because radial CAIPI inherits the advantages of radial k-space trajectories, reduced field-of-view phantom and human images were acquired with no additional increase in scan time. Finally, the use of golden angle radial CAIPI provided flexibility in view-sharing reconstruction.

Conclusions: Radial CAIPI permits rapid and robust separation of simultaneously excited slices without the need for differences in coil sensitivities or use of parallel imaging reconstruction techniques, facilitating acceleration of cine imaging for exception gating and dynamic MLC tracking on MRI-gRT systems. Future work will combine radial CAIPI with in-plane radial undersampling to achieve higher acceleration factors to increase temporal resolution.

DAY 1, 16:10–16:25

MR IMAGING IN PEDIATRIC EPENDYMOMA : WHAT DO WE GAIN FOR RADIOTHERAPY OUTCOME AND PREDICTION OF RELAPSE SITE?*

Tensaouti.F[1], Ducassou. A[3], Liceaga S[1]. Lotterie. J.A1,[2], Sevely[2]. A, Peran. P[1], Berry. I1,[2], Celsis. P[1], Laprie. A[1, 2]

(1) INSERM, UMR 825, Toulouse, F-31059 France
(2) CHU Toulouse, F-31059 France
(3) Institut Claudius Regaud de lutte contre le cancer, Toulouse, F-31059 France

Introduction: Ependymoma is the third most common primary brain tumor in children. Radiotherapy (RT) is systematically delivered after surgery. However, more than a third of children experience relapse locally or around the resection cavity. In the absence of a prospective clinical trial in Europe, we conducted a national retrospective study on children with newly diagnosed intracranial Ependymoma treated with post-operative RT between January 2000 and December 2013. The aim of this study was to investigate if Perfusion MRI (by Dynamic Susceptibility Contrast, DSC) and diffusion-weighted imaging (DWI), can help us predict RT outcome by identification of site of relapse and significant sub volumes of tumors related to treatment outcomes in a dose-painting approach perspective.

Material and method:211 patients were included in Imaging data from 114 patients could be retrieved. Among them, 12 had DSC MRI and 44 DWI MRI at pre radiotherapy exam. For each patient, GTV were delineated in postcontrast T1 WI before radiotherapy. The relapse volume (RV) was delineated in postcontrast T1 WI at relapse . Initialy, RV was compared with the GTV, with boolean operator . In a second time, the GTV was mapped to the coregistered rCBV map and ADC map. Then an histogram analysis was done to determine for rCBV and ADC the best fitting of the GTV data histogramm with 2 or 3 Gaussian functions. According to the fitting results, the GTV was then partitioned into 2 or 3 spatial subvolumes using an automatic clustering method (Isodata algorithm). Each subvolume with the lower CBV was normalized to the GTV volume and evaluated for its association with outcome and prediction of the relapse site. All image analysis were completed using OLEA software for CBV analysis and an in-house software package Sysiphe for volumes analysis.

Results: 40% patients presented with relapse. Recurrences were mainly local (strictly local in 66% of recurrences, local and distant in 23 % and strictly distant in 11%). 24 patients had T1 WI at pre radiotherapy and at relapse. Results showed that 60 % of relapse volume was located in GTV volume.The percentage of the subvolumes with low CBV in GTV, without cavity resection, were significantly greater, in the 6 patients with LF than 6 with LC (respectively 63.41% versus 44.99 %, p = 0.03). The positive predictive value (VPP) of the low CBV volume for relapse site was low, although, greater than the hyperperfused volume (respectively VPP 5 % with sensibility of 55.71 % versus VPP = 3.31 and sensibility =18.68 %).

Conclusion: Although, the low CBV volumes were not clearly predictive for relapse site, the proportion of low CBV volumes appeared as a predictive factor of outcome after radiotherapy in pediatric ependymoma . This is a promising finding as radio resistance resulting from hypoperfusion and consequent hypoxia could be overcome by increasing radiation dose to a higher-risk population. Our study is in progress, we are currently investigating the added value of diffusion MRI in the prediction of relapse site on a larger cohort of 44 patients.

DAY 2, 9:00–9:15

TREATMENT RESPONSE ASSESSMENT WITH ADC FOR CHEMORADIATION OF PANCREATIC ADENOCARCINOMA*

Entesar Dalah, An Tai, Kiyoko Oshima, William A Hall, Eric Paulson, Beth Erickson, X Allen Li
Medical College of Wisconsin

Purpose: To investigate the correlations of apparent diffusion coefficient (ADC) values obtained from diffusion weighted MRI (DW-MRI), PET and pathological data in pancreatic adenocarcinoma treated with neoadjuvant chemoradiation (nCR).

Materials/Methods: MRI, PET, and pathological data collected for a total of 16 patients with resectable, and borderline resectable pancreatic adenocarcinoma treated with nCR were retrospectively analyzed. All patients were treated with IMRT to 50.4 Gy at 1.8 Gy per fraction with Gemcitabine or Xeloda based chemotherapy before surgery. While all 16 patients had DW-MRI scans post nCR (on average one month after nCR), only 12 had pre- and post-nCR DW-MRI scans, among whom 11 had pre- and post-nCR PET scans. Surgical specimens were graded according to tumor cell destruction (cellularity), with Grade 1 (G1) for good response (single cells or small groups of residual cancer cells in extensive fibrosis), Grade 2 (G2) for moderate response (residual cancer outgrown by fibrosis), and Grade 3 (G3) for poor response (extensive residual cancer). For the patients analyzed, 3 cases were classified as G1, 10 as G2, and 3 as G3. Gross tumor volumes (GTV) for each patient were manually delineated on the corresponding ADC parameter maps (GTVADC). The histogram of ADC values in all the voxels inside the GTVADC were used to calculate the mean and minimum ADC values and the standard deviation (SD). A 2-component Gaussian fitting of the post ADC histogram was used to separate the cellularity and fibrosis regions inside the GTVADC. Pre- and post nCR mean GTVADC, ADC values, lean body mass normalized SUV (SUVlb) were compared using a Mann-Whitney test. Post nCR ADC, SUVlb, and tumor maximum dimension (TMD) were correlated with pathological treatment response (PTR), and pathological size (PS) using Pearson's correlation coefficient test.

Results: A significant increased post-nCR mean ADC values (1.674±0.181×10-3 vs 1.376±0.093×10-3 and significant decreased GTVADC (10.07± 5.77 cm3 vs 19.58±11.55 cm3) (P=0.0204) were observed in the 12 patients studied. The mean and minimum ADC values after nCR were significantly correlated with the PTR (R2=- 0.5092); P=0.0057, and (R2=- 0.6421); P=0.0002, respectively. The PET-SUVlb were not significantly correlated with PTR (R2=0.5629); P=0.0687 in the 11 patients studied. Post- ADC and SUVlb were weakly correlated (R2=-0.1515; P=0.6821). The mean difference in TMD measured from ADC, and SUVlb as compared with PS were 0.75, and 0.41 cm, respectively. The average mean and SD of the ADC values in the ADC-defined cellularity and fibrosis regions were (1.801± 0.116×10-3) and (2.039± 0.250×10-3) for the G1 cases, (1.559±0.130×10-3) and (1.736± 0.218×10-3) for G2, and (0.322±0.383×10-3) and (1.253±0.893×10-3) for G3, respectively. For post-nCR ADC and SUVlb, 5/11 showed agreement between ADC, SUVlb and PTR, 2/11 SUVlb agreed with PTR, and 2/11 ADC agreed with PTR.

Conclusion: Post treatment ADC values were found to be strongly correlated with pathological treatment response (cellularity) for pancreatic adenocarcinoma patients treated with chemoradiation therapy, indicating that ADC acquired following a course of chemoradiation could be used to predict tumor pathologic response and improve the selection of patients who could preferentially benefit from therapeutic intensification.

DAY 2, 9:15–9:30

ANALYSIS OF MULTI-PARAMETRIC MRI AT 3.0 TESLA FOR THE PREDICTION OF TREATMENT RESPONSE IN RECTAL CANCER.*

Trang Pham[1,2,3], Gary Liney[1,2,3,4], Dale Roach1, Karen Wong[1,2,3], Daniel Moses[2], Benjamin Schmitt[5], Michael Barton[1, 2,3].

(1) Ingham Institute for Applied Medical Research, Liverpool, Sydney, Australia
(2) Liverpool Cancer Therapy Centre, Liverpool Hospital, Liverpool, Sydney, Australia
(3) Faculty of Medicine, University of New South Wales, Australia
(4) Faculty of Radiation Physics, University of Wollongong, Australia
(5) Siemens Healthcare Ltd Australia

Introduction/Purpose: Current functional MRI techniques have shown promising results for prediction of response to chemoradiotherapy (CRT) in rectal cancer, but lack sufficient accuracy for clinical use. There is a wide variation in performance of functional MRI in response prediction reported. Most studies describe single parameter values from either diffusion or perfusion MRI. Single parameter measurements, such as mean ADC or Ktrans, do not reflect tumour heterogeneity. The purpose of this study was to develop a robust methodology for the assessment of quantitative diffusion weighted imaging and dynamic contrast enhanced (DCE) imaging used in combination to predict treatment response in rectal cancer. This study combines the latest imaging protocol and analysis strategy to assess tumour heterogeneity and its changes in response to CRT.

Methods/Materials: Patients with locally advanced rectal cancer undergoing neoadjuvant CRT prospectively underwent MRI on a 3T wide bore Siemens Skyra at 3 time-points: Pre-CRT, week 3 CRT, and post-CRT. The study protocol consisted of: (i) T2-weighted images (ii) DWI using RESOLVE, which we have previously shown to be robust with respect to geometrical distortions1. Images were acquired with b-values 50 and 800s/mm2 and 1 & 3 averages. ADC maps and calculated b=1400s/mm2 images were produced as part of protocol (iii) DCE consisted of pre-contrast VIBE scans with flip angles 2º and 15º in order to calculate native T1, followed by gadoversetamide (0.1mM/kg) injection and 60 phases using TWIST with a 5s temporal resolution. For DCE analysis, the flip angle images were registered to DCE images using rigid body registration. Tissue4D was used to produce Ktrans maps by first pre-selecting an appropriate arterial input function, scaled by dose, based on chi-squared goodness of fit. Multi-parametric histogram analysis was performed using OncoTreat (WIP). Parameter maps were registered to T2-weighted images. Segmentation was used to define the volume of interest from hyperintense tumour on the b-value=1400 images. A voxel-by-voxel technique was used to produce histograms of ADC and Ktrans. Data was displayed as colour-coded maps and histograms side-by-side, as well as combined scatterplots and difference histograms for both parameters at each time-point. CRT response was defined according to histopathology tumour regression grade.

Results: A complete protocol and analysis strategy was successfully developed which has utilized commercial, in-house developed and works-in-progress (OncoTreat) software. We found the calculated b-value=1400 images useful for visualization of tumour. For DCE analysis, pre-registration of flip angle to dynamic images was a crucial step in producing pixel-by-pixel T1 map, to ensure accurate voxel-by-voxel calculation of Ktrans and had to be performed outside of commercial software owing to its limitations. In CRT responders, the week 3 histograms and maps showed a shift in distribution of ADC of pixels to higher values and Ktrans of pixels to lower values compared to the pre-CRT histogram.

Conclusions/Discussion: Multi-parametric histogram analysis of ADC and Ktrans appears to be a promising and feasible method of assessing tumour heterogeneity and its changes in response to CRT in rectal cancer. We are presently continuing this work in a larger cohort study.

[1]Liney et al. BJR. http://dx.doi.org/10.1259/bjr.20150034

DAY 2, 9.30–9:45

ASSESSMENT OF DIFFUSION-WEIGHTED IMAGING AND R2* MEASUREMENTS WITH 18F-FDG-PET IN HEAD AND NECK CANCER PATIENTS TREATED WITH RADIATION THERAPY *

Myo Min, Gary Liney, Peter Lin, DJ Wijesekera, Mark Lee, Lois Holloway, Dinesh Gooneratne, Robba Rai, Allan Fowler, Dion Forstner
Ingham Institute, Australia

Background: There is a growing role of the use of functional imaging for prognostic stratification of head and neck cancer (HNC). FDG-PET although well investigated has limitations with respects to spatial resolution. Functional MRI can overcome some of the disadvantages of PET imaging by reducing radiation exposure to the patient, being able to image different biomarkers in the one session and having high anatomical spatial resolution. Non-contrast studies have a relatively short scan time and are ideal for serial assessment of tumour response to treatments. Diffusion-Weighted-Imaging (DWI) and R2* have the potential to measure different tumour factors such as changes in tumour cellularity and oxygenation within the tumour. These changes occur during radiotherapy treatment, and assessment of these factors may help identify tumours with a higher or lower risk of recurrence. The aim of the study was to evaluate serial changes, and correlate DWI and R2*-MRI with FDG-PET when assessed before and during radiation therapy (RT).

Materials and methods: Patients with newly diagnosed biopsy-proven mucosal primary HNC, suitable for radical RT were prospectively recruited. FDG PET-CT was acquired on a GE Discovery-710 PET-CT before (pre-PET) and at the 3rd week of RT (iPET). MRI was performed on a dedicated wide bore 3.0 Tesla scanner (MAGNETOM Skyra, Siemens AG, Erlangen, Germany) before and during RT at 2nd, 3rd, 5th and 6th weeks of treatment. Sequences obtained were: DWI using RESOLVE (acquired at b=50 and 800 s/mm2) and a multiple gradient echo for the calculation of R2* using 8 echoes (TE= 5 to 74 ms). Pixel-by-pixel maps of apparent diffusion coefficient (ADC) and R2* were calculated using the scanner console and ImageJ respectively. FDG-PET metabolic parameters obtained were: maximum standardized-uptake-value (SUVmax), metabolic-tumour-value (MTV) and total-lesional-glycolysis (TLG). Assessments of the primary tumour were made using the PET-VCAR (Volume-Computer-Assisted-Reading) software. Pearson correlation test (two-tailed) was used to evaluate correlations between mean ADC values, R2* values and FDG-PET metabolic parameters (SUVmax, MTV and TLG).

Results: A total of 27 patients received pre-treatment scans and 18 patients received mid-treatment scans. Pre-treatment R2* values were negatively correlated with all three pre-PET metabolic parameters: SUVmax (p=0.01); MTV (p=0.02); and TLG (p=0.05). In addition, R2* values from the 3rd and 5th week of RT were again negatively correlated with iPET MTV (p=0.05, 0.02 respectively) and TLG (p= 0.07, 0.04 respectively). No significant correlation was found between the mean ADC values and either R2* values or FDG-PET metabolic parameters. Significant differences ($p<0.05$) in ADC values were observed from pre-RT to each of the time points studied. The difference in mean ADC values increased with time to week 5 (mean difference: -199, -311, -395, and -374 in week 2, week3, week 5 and week 6 respectively).

Conclusion: Changes in pretreatment and mid-treatment ADC values are measurable in patients with HNC undergoing RT. Pre-treatment and mid-treatment (3rd and 5th week) R2* values were significantly correlated with metabolic parameters of pre-PET and iPET respectively. Further evaluation of the role of these changes to assess correlation with local failure is currently being performed.

DAY 2, 9:45–10:00

WEEKLY RESPONSE ASSESSMENT OF INVOLVED LYMPH NODES TO RADIOTHERAPY USING DIFFUSION WEIGHTED MRI IN OROPHARYNX HEAD AND NECK SQUAMOUS CELL CARCINOMA (HNSCC)

Neelam Tyagi PhD, Nadeem Riaz MD, Vaios Hatzoglou MD, Robert Young MD, Kenneth Wengler, James Mechalakos PhD, Amita Dave PhD, Margie Hunt MS and Nancy Lee MD
Memorial Sloan-Kettering Cancer Center

Introduction/Purpose: Oropharynx patient population is known to have a favorable prognosis, making them an ideal candidate for adaptive therapy. A re-plan to improve coverage or escalate/de-escalate dose based on morphological information alone may not be adequate as the grossly involved lymph nodes (LN) of a subset of these patients tend to become cystic that often do not regress. Functional adaptation is a better approach when considering re-planning for these patients. The purpose of this study was to evaluate the weekly trends in treatment related morphological and physiological changes for these LNs using DW-MRI and evaluate its implications for adaptive re-planning.

Methods/Materials: Ten patients with histologically proven oropharynx HNSCC undergoing concurrent chemo-radiation were analyzed in this study. MR imaging protocol included axial T1w, T2w and DW-MRI using a 3 Tesla Philips MR scanner. The patients were scanned weekly in radiation treatment planning position using a 16 element phased-array anterior coil and a 44 element posterior coil. A total of 65 DWI and T2w scans were analyzed. DWI was performed using an optimized single-shot echo planar imaging sequence (TR/TE = 5000/65 ms, slice thickness = 5mm; slices=28; b values = 0 and 800 s/mm2). Quantification of the DW-MRI images was performed by calculating the apparent diffusion coefficient (ADC). T2w and DWI scans were imported into Eclipse treatment planning system and gross tumor volumes (GTVs) corresponding to involved LNs was contoured on each axial slice by two expert physicians. An attempt was made to remove any cystic or necrotic components such that the ADC analysis was of viable tumor only. A pixel-by-pixel fit within the GTVs was calculated using monoexponential behavior of signal intensities. From each GTV histogram mean, median, standard deviation, skewness and kurtosis were calculated. Absolute and % change in weekly ADC histogram parameters as well as % change in T2w GTV volumes were also calculated.

Results: For all nodes, an immediate change in ADC was observed during first 2-3 weeks after which ADC values either continues to increase or plateaus. A few nodal volumes had a slightly decreased ADC value during later weeks. Percent increase in median ADC from weeks 1 through 6 with respect to baseline were 15%, 23%, 42%, 42%, 44% and 60%. The corresponding change in median T2 volumes were 8%, 10%, 16%, 22%, 40% and 42% respectively. The ADC distribution of the viable tumors was initially highly kurtotic however, the kurtosis decreased as treatment progressed. The ADC distribution also showed a higher degree of skewness in the first 2 weeks, progressively becoming less skewed as treatment progressed so as to slowly approach a more symmetric distribution.

Conclusions: Physiological changes in LNs represented by changes in ADC evaluated using DW-MRI are evident sooner than the morphological changes calculated form T2w MRI. The decisions for adaptive re-planning may need to be individualized and should be based primarily on tumor functional information. Our data also suggest that for many patients, week's 3-4 maybe the optimal time to intervene and re-plan. Larger studies are needed to confirm our findings.

DAY 2, 14:45–15:00

TOWARDS INTER AND INTRA FRACTION PLAN ADAPTATION FOR THE MR-LINAC*

C Kontaxis, G H Bol, J J W Lagendijk, B W Raaymakers
University Medical Center Utrecht, Utrecht, The Netherlands

Introduction/purpose: To develop a new sequencer for IMRT that during treatment can account for anatomy changes provided by online and real-time MRI. This sequencer employs a novel inter and intra fraction scheme that converges to the prescribed dose without a final segment weight optimization (SWO) and enables immediate optimization and delivery of radiation adapted to the deformed anatomy.

Methods/materials: The sequencer is initially supplied with a voxel-based dose prescription and during the optimization iteratively generates segments that provide this prescribed dose. Every iteration selects the best segment for the current anatomy state, calculates the dose it will deliver, warps it back to the reference prescription grid and subtracts it from the remaining prescribed dose. This process continues until a certain percentage of dose or a number of segments has been delivered. The anatomy changes that occur during treatment require that convergence is achieved without a final SWO. This is resolved by adding the difference between the prescribed and delivered dose up to this fraction to the prescription of the subsequent fraction. This process is repeated for all fractions of the treatment.

Results: Two kidney cases were selected to test the pipeline by producing artificial intra fraction baseline shifts in the cranial-caudal direction. For each case, a set of intra fraction anatomies was produced featuring a gradual shift of the target. For the first kidney case, with a GTV volume of 2.3 ml and a maximum shift of 1 cm after 49 segments, the dose convergence of the adaptive scheme at the end of the treatment fraction, relative to the prescribed dose was 7.5% higher than the static plan delivered to the respective deformed anatomies. For the second kidney case, with a GTV volume of 9.1 ml and a maximum shift of 1.3 cm after 67 segments, the adaptive scheme was 7.3% higher than the static plan at the end of the treatment fraction.

Conclusions/discussion: This new adaptive sequencing strategy enables dose convergence without the need of SWO while adapting the plan to intermediate anatomies, which is a prerequisite for online plan adaptation. We have demonstrated that our sequencer is able to adapt the plan to anatomy baseline shifts during treatment and ensure dose convergence without the use of extra margins around the GTV.

DAY 2, 15:00–15:15

BENCHMARK AND VALIDATION OF MONTE-CARLO MODELS FOR RADIATION DOSIMETRY IN B-FIELDS

JA de Pooter[1], S Duane[2], H Bouchard[2]

(1) VSL B.V., Thijsseweg 11, NL-2629 JA Delft, The Netherlands
(2) National Physical Laboratory, Teddington, United Kingdom

Purpose: With the advent of MRI-guided radiotherapy, radiation dosimetry in the presence of magnetic fields (B-fields), as part of the QA for these new modalities, must be addressed in several ways to assure accurate dose delivery and patient safety. To calculate dose in the presence of B-fields, Monte Carlo is recognized as the most promising method for its ability to simulate charged particles transport in detail. At the present time, general-purpose codes such as PENELOPE and GEANT4 already offer this option and other codes, such as EGSnrc, remain under development. Since the classical Fano test cannot be applied in such conditions, the accuracy of Monte Carlo dose calculation in the presence of B-fields is currently unknown. , Therefore, a suitable method for validating Monte Carlo algorithms in conditions relevant to MRI-guided radiation dosimetry is required. This study proposes a method to apply the Fano cavity test and presents its first application to benchmark Monte Carlo simulations of ionisation chamber response in the presence of an external B-field.

Methods: The proposed method is based on Fano's approach to achieve charged particle equilibrium in heterogeneous media having uniform atomic properties. Based on the Boltzmann radiation transport equation, modified to include the Lorentz force, it is shown, that to apply the Fano test to a cavity in the presence of a B-field, the condition of isotropy of the secondary electron fields (Charged Particle Isotropy, CPI) is required. The Fano test is applied to a Monte Carlo model using the PENELOPE code. Simulations are performed with a uniform B-field B = 1.5 T and B = 0.0 T for a cylindrical cavity geometry. The secondary particle field consists of electrons generated from mono-energetic sources (E = 0.5 – 4.0 MeV) with a uniform source density and different angular distributions; isotropic (CPI), mono-directional (no-CPI), and Compton (no-CPI).

Results: Results are presented as the ratio between dose to the cavity and the average energy per unit mass of the secondary particle field. For the angular distributions violating the CPI condition and B = 1.5 T, the deviations from 1 are considerable (12%). Results for the isotropic distribution for B = 1.5 T show agreement with the Fano test to a level of 0.3 % for most energies. For some energies, there is a significant deviation, which is similar to the deviations seen for the simulations with the same energies for B = 0.0 T.

Conclusion: While it was previously shown that in general, Fano's theorem cannot hold in the presence of a B-field, this study is a significant improvement towards benchmarking the accuracy of Monte Carlo codes coupling radiation transport to external B-fields. CPI is an essential condition for assessing the accuracy of Monte Carlo transport codes in the presence of B-fields. Due to the deviations observed for B = 0.0 T, a final conclusion on the accuracy of the PENELOPE code for the simulation of detector response in the presence of B-fields requires further investigation.

DAY 2, 15:15–15:30

AN ONLINE ADAPTIVE REPLANNING PROCEDURE FOR MR-LINAC

Ozgur Ates, Ergun E. Ahunbay, and X. Allen Li
Medical College of Wisconsin

Introduction/purpose: Integrated MRI and Linac (MR-Linac) system may delivery radiation therapy via IMRT and VMAT using flattening filter free (FFF) beams with couch lateral motion prohibited. In such a system, patient translational errors may be corrected by shifting MLC, termed virtual couch shift (VCS). For FFF beams, VCS would result in degraded dose distribution due to the beam unflattening. Here, we introduce a fast replanning method that can address this beam unflattening issue and can be implemented in conjunction with VCS on the MR-Linac system.

Methods/materials: The method include 2 steps: (1) using a warm-start optimization (WSO) to generate a series of plans (e.g., segment apertures and MUs) at a series of shifts from VCS to eliminate the adverse dose effects of FFF beams, and (2) using a segment aperture morphing (SAM) algorithm modified for both IMRT and VMAT to correct for target deformation. To implement, WSO can be executed offline starting with the original plan (rather than starting from scratch) using the original anatomy and objective functions. At a treatment fraction, a plan from WSO will be selected based on the shift determined for VCS from the anatomy of day, or the interpolated MLC positions and MU's, then SAM will be applied to change the MLC positions based on the change of BEV of the target from the images (MRI or CT) of the day. The process, requiring no online plan optimization and dose calculation, can be executed rapidly (< 10 min with a hardware of 16-CPU, 2.6 GHz dual core). The process was implemented on a research MR-Linac planning system (Monaco, Elekta) and was tested with MRI and CT data sets for representative prostate and pancreas cancer cases. For a given daily image set (CT or MRI), three plans from VCS alone, VCS+SAM, and VCS-+WSO+SAM were generated to correct for translational shifts, translation shifts + target deformation, and translational shifts + target deformation + beam unflattening, respectively. Note that the WSO were performed offline based on planning images. These three plans were compared with each other and with the fully-optimized plan based on the daily images (golden standard) using on a series of dose-volume parameters.

Results: For three prostate cases examined, the average PTV-V100(%)/CTV-V100(%)/CTV-Dmin(Gy) are: 90.0(±5.0)/96.4(±0.7)/58.5(±3.1), 92.5(±4.2)/99.3(±0.2)/71.6(±2.0), 93.4(±3.6)/99.4(±0.8)/73.3(±1.7) and 96.2(±2.3)/99.9(±0.1)/75.0(±1.6) for VCS alone, VCS+SAM, VCS+WSO+SAM, and the golden standard, respectively. These values for two pancreas cases studied are: 89.0(±6.3)/97.4(±0.1)/41.3(±1.0), 96.9(±0.1)/98.5(±0.3)/42.5(±0.3), 97.3(±0.5)/98.6(±0.1)/43.5(±0.6) and 99.4(±0.5)/99.8(±0.2)/50.5(±3.2). These data demonstrate that the proposed method of using offline SWO and online SAM can effective consider the effects from the beam unflattening and interfractional variations.

Conclusions/discussion: The introduced adaptive replanning procedure can fully address interfractional variations and beam unflattening without the need of patient repositioning. This procedure can be performed practically fast and may be used for online replanning for certain MR-Linac systems, where couch lateral shift is prohibited due to the limitation from MRI acquisition.

DAY 2, 15:30–15:45

MINIMAL INTERFERENCE FROM LINAC COMPONENTS ON MAGNETIC FIELD HOMOGENEITY IN 1.5T MR-LINAC

Tiina Näsi, Panu Vesanen, Aleksi Halkola, Juha Oila, Tero Virta, Jukka Tanttu, Jarmo Ruohonen, Johan Overweg
Philips Healthcare

Introduction: An MR-Linac system acquires magnetic resonance (MR) images before, during and after radiotherapy (RT) treatment to aid in targeting the treatment accurately and to follow up the treatment response. During RT, a linear accelerator (Linac) rotates around the MR subsystem and delivers radiation through it. The Linac gantry is located close to the MR subsystem, thus potentially affecting the magnetic field (B0) homogeneity essential for MR imaging. The purpose of this study was to investigate the image quality of an industry-built 1.5T MR-Linac with B0 and power-on measurements as well as with volunteer imaging.

Methods: The measurements were performed with a 1.5T MR-Linac system that has been designed to minimize interference between MR and Linac subsystems so that the radiation beam attenuation is low within the MR subsystem and the stray magnetic field small in the vicinity of the gantry. The effect of the gantry on B0 was measured from phase images with 60° increments in the gantry angle. The tested gantry contained most of its components. Of the remaining components, the multi-leaf collimator (MLC) was estimated to have the largest influence on B0. Its effect was studied separately with and without the component attached near the MR cryostat. Additionally, hysteresis was investigated by rotating the gantry several times in opposite directions. Components on the gantry were powered on during ghost, spike and radio-frequency noise scans to see if powering the components affected the image quality. Two volunteers were scanned with a near-real-time sequence envisaged suitable for RT treatment monitoring purposes (2D balanced SSFP, bandwidth 1076 Hz/pixel, pixel size 3x3 mm2, scan time 0.2 s/image) during rotation (1 rpm) of the gantry. The same sequence was repeated at Ingenia 1.5T scanner with a similar setup for comparison.

Results: Inside a sphere with a diameter of 350 mm, the peak-to-peak B0 inhomogeneity caused by the populated Linac gantry (MLC and some other components missing) was 340 nT in the central axial plane (corresponds to 0.1 mm distortion at 150 Hz/mm bandwidth envisaged for RT online planning sequences). The inhomogeneity was approximately linear and fixed with respect to the angular position of the gantry. No hysteresis was observed. The MLC caused a peak-to-peak effect of 940 nT (0.3 mm at 150 Hz/mm bandwidth) in the central axial plane. Optimized passive shimming was able to reduce the B0 inhomogeneity by a factor of five. No adverse effects on the image quality were observed when scanning while the gantry components were powered.Visual inspection of the volunteer images showed no noticeable effect in the image quality when the populated gantry with 340 nT B0 inhomogeneity was rotated during imaging.

Conclusion: The rotating gantry of a 1.5T MR-Linac with tested components does not significantly affect the image quality of sequences planned for RT beam-on imaging purposes. The static gantry has a negligible effect on image distortion in sequences envisaged for online RT planning.

DAY 2, 15:45–16:00

REAL-TIME TUMOR MOTION TRACKING IN LOW FIELD CINE-MR IMAGES USING PRINCIPAL COMPONENT ANALYSIS*

Hanlin Wan, Robert Pless, Parag Parikh
Washington University School of Medicine

Purpose: ViewRay's MRIdian system acquires cine-MR images during treatment, allowing for real-time visualization of the tumor without additional dose. We propose a novel method for tracking the tumor target on these cine-MR images in real-time.

Methods/Materials: 9 patients with mobile abdominal tumors (3 stomach, 1 pancreas, 1 adrenal, 2 mesenteric, 2 peritoneal) were imaged on ViewRay (0.3T, open-bore; TrueFISP). Sagittal slice cine-MR images (3.5x3.5mm pixels) were acquired at 4 frames per second. A 25-second training period was used to collect 100 images during normal breathing. Principal component analysis (PCA) was used to bin the images using the first 2 eigenvalues. Manual contouring of the target was performed one image. The mean eigenvalues in each bin were used to reconstruct 15 images, on which template matching to the hand-drawn contour was used to locate the target. A linear fit of the pixel locations was used to create the motion model. For each subsequently acquired image, the 2-component PCA model was inverted and the values plugged into the motion model to get the corresponding pixel location. Finally, this location and the user-drawn contour were used as the initialization for an active contouring algorithm to refine the edges of the tracked target. 100 images for each patient were manually contoured and used as the gold standard for comparison using the Dice similarity coefficient (DSC) and the modified Hausdorff distance (MHD).

Results: The mean DSC is 0.87±0.09 and MHD is 2.6±0.9mm, which is less than the pixel size. The algorithm takes 100ms per image using Matlab, and is therefore more than fast enough for real-time use.

Discussion/Conclusions: We have developed a novel and robust method for real-time tumor motion tracking in low-resolution, low-field cine-MR images. Typical tracking algorithms make assumptions about the allowed motion space and can therefore result in erroneous tracking when large, unexpected motions occur, such as the patient coughing. By comparing each image to the reconstructed image from our PCA model, we can easily detect such errors. We are currently looking into using our method for automated gating and dosimetric measurement purposes with the ViewRay system.

CLINICAL IMPLEMENTATION OF 4DMRI

Carri K. Glide-Hurst1[,2], Joshua Kim[1], David To[1, 2], Tim Nielsen[3], Mo Kadbi[4], Yanle Hu[5], Indrin J. Chetty[1, 2]

(1) Department of Radiation Oncology, Henry Ford Health System, 2799 West Grand Boulevard, Detroit, Michigan 48202
(2) Department of Radiation Oncology, Wayne State University, 4100 John R, Detroit, Michigan 48202
(3) Philips Healthcare, Hamburg, Germany
(4) Philips Healthcare, Cleveland, OH
(5) Department of Radiation Oncology, Mayo Clinic Arizona 5777 E MAYO Boulevard, Phoenix, AZ 85054

Introduction/purpose: Precise radiation therapy (RT) for abdominal lesions is complicated by respiratory motion and suboptimal soft tissue contrast from 4DCT whereas 4DMRI provides superior tissue discrimination. This work develops a suite of tools for clinical implementation of a novel 4DMRI algorithm and evaluates its performance in human subjects including the incorporation of visual biofeedback (VBF) for motion management in RT.

Methods/materials: Prospective respiratory-triggered, T2-weighted coronal 4DMRIs were acquired on an open 1.0T MR-SIM on an IRB-approved protocol. An external surrogate (respiratory bellows) was used for breathing waveform generation. An automated MATLAB® (Mathworks, Natick, MA) toolkit was developed to perform the following tasks: sort the images into bins according to phase numbers identified in the DICOM header, reorder data according to recorded slice position, and generate derivative images (maximum, minimum, and average intensity projections (MIP, MinIP, and AVG, respectively)) in a manner analogous to 4DCT. Fifteen 2-8 phase 4DMRI scans were acquired in 5 healthy volunteers and 2 patients with typical parameters of TE/TR/echo shot = 75-90ms/3500-4500ms/305-360ms. Normalized respiratory waveforms were evaluated for scan time, duty cycle (programmed/acquisition time), breathing period, end-inhale (EI) amplitude and breathing variability (coefficient of variation, EI-COV). Maximum intensity projections (MIPs) were analyzed. To quantify the impact of VBF on scan time and respiratory waveform, 8 healthy volunteers were scanned with and without an MR-compatible interactive breath-hold control system that was calibrated at end-exhale. Subjects monitored their breathing patterns for 2-8 phase 4DMRI acquisitions and differences with and without VBF were assessed.

Results: The 4DMRI toolkit was utilized by several users and found to be robust. Code modifications were needed when MRI datasets were archived as compared to those sent via DICOM filter directly from the scanner. A strong, positive association was observed between 4DMRI acquisition time and breathing rate (Pearson r ~0.8). The longest acquisition (16.6 minutes) occurred for a 6-phase 4DMRI for an irregular breathing volunteer with breathing rate of 7.0 bpm, whereas an abdominal cancer patient breathing with regular periodicity at 17.8 bpm had a 7.1 minute 8-phase acquisition. Using VBF yielded higher duty cycles than free breathing (34.7% versus 28.3%, respectively) while reducing 8-phase acquisition time by 1.7±1.2 minutes. EI-COVs were reduced by almost 50% when VBF was implemented. The overall breathing amplitude increased with VBF (0.84±0.05 a.u. with versus 0.72±0.06 a.u. without).

Conclusions/discussion: 4DMRI offers potential for motion management in RT although as expected, irregular breathing patterns and slow breathing rates adversely impacted acquisition efficiency. Incorporating VBF improved acquisition times and breathing reproducibility although the overall breathing amplitudes also increased. This suggests that VBF would need to be implemented throughout the entire clinical workflow. Further efforts to improve acquisition efficiency such as incorporating compressed sensing or a more robust surrogate used for triggering are desirable.

DEVELOPMENT OF A PHANTOM AND METHOD TO ALIGN MR AND MV CO-ORDINATES SYSTEMS ON A MR-LINAC

M Sell[1], J.G.M Kok[2], S Crijns[2], M Glitzner[2], J Byrne1, J Harasimowicz[1], D A Roberts[1]

(1) Elekta Ltd., Linac House, Fleming Way, Crawley, West Sussex, United Kingdom
(2) University Medical Center Utrecht, Heidelberglaan 100, 3584 CX Utrecht, Netherlands

Purpose: Image guided radiotherapy requires alignment of the coordinate systems of both the imaging and radiation treatment modalities. In the case of Elekta's Atlantic system the coordinate systems of the magnetic resonance imaging system and megavoltage beam need to be aligned. This work develops a phantom and software analysis package to determine the rigid transformation between the MV and MR coordinates.

Methods: A phantom has been developed which consists of eight ZrO2 spheres surrounded by plastic and water. These non-magnetic, non-conductive ceramic markers of a relatively high atomic number can be detected in the MV images without introducing artifacts and distortion to the MR modality. At the same time, the liquid surrounding the markers is visible in the MR images. Hence, the spheres provide landmarks visible in both MR and MV cone beam CT images. In-house developed software was applied to detect sphere centers in 3D space in both sets of images. The detection method calculates the intensity gradient for each voxel and draws lines along the gradient direction if certain criteria are met. Afterwards, the sphere centers are detected and stored. Corresponding pairs of coordinates are determined in the two sets of images based on the known geometry of the phantom. Finally, a rigid transform is applied to the MR coordinates to align it relative to the megavoltage system. To mitigate the influence of detection uncertainties, the transform is determined by minimizing the sum of distances between the corresponding coordinates. In a proof-of-concept study, MR images were acquired at the MR Linac experiment at UMC, Utrecht, Netherlands, and MV CBCT images were acquired using an Elekta Precise Linac fitted with iView GT.

Results: The average magnitude of the error vector between the MR and MV landmark coordinates was 0.34 mm. The largest error 0.69 mm. The disagreements are partially caused by the phantom prototype being 3D printed, which introduces mechanical tolerances between the MR marker center defined by the plastic surrounding the ZrO2 spheres visible in MV CBCT images. The final design will be produced with higher precision.
Based on these results the phantom geometry has been improved. Once this phantom is available, further studies, e.g. on the influence of different imaging parameters on the detection accuracy, will be performed.

Conclusions: A prototype phantom has been developed to enable the alignment of the MR and MV coordinate systems. It was demonstrated that the MV and MR coordinate systems can be aligned to each other to within 0.34 mm on average. This work demonstrates that the MR imaging and megavoltage therapy beam can be accurately aligned allowing for accurate MR guided radiotherapy.

REPRODUCIBILITY OF ARTERIAL INPUT FUNCTION OF DCE-MRI IN PROSTATE CANCER: INFLUENCE OF VARYING INJECTION DURATION*

E.M.E. Klawer[1], P.J. van Houdt[1], F.J. Pos[1], H.J. Teertstra[2], U.A. van der Heide[1]

(1) Department of Radiation Oncology, the Netherlands Cancer Institute, Amsterdam, the Netherlands
(2) Department of Radiology, the Netherlands Cancer Institute, Amsterdam, the Netherlands

Purpose: Dynamic contrast-enhanced (DCE) imaging enables quantification of tissue perfusion and permeability with pharmacokinetic analysis (PKA). However, resulting PKA parameters differ between and within institutes[1] and modalities (i.e. DCE-CT and DCE-MRI)[2]. One input parameter that influences the results is the arterial input function (AIF)[3]. The aim of this study is to determine the influence of overall injection duration on the AIF taking intra-patient variability into account.

Method: Patients with prostate cancer from two study populations were included. The first group underwent DCE-MRI twice with the same protocol and an overall injection duration of 5s (n=8). The second group of 30 patients received two DCE-MRI examinations with an injection time of 5s in the first exam and a prolonged injection time in the second exam: 7.5s (n=8), 10s (n=8), 15s (n=5), 20s (n=4) and 30s (n=5). The total injected volume of contrast agent was 7.5mmol gadolinium (15ml, 0.5mM Dotarem). The DCE exam was carried out on a 3T MR scanner (Achieva, Philips, the Netherlands) using a T1-weighted 3D spoiled gradient echo sequence (300s duration, time interval of 2.5s). AIFs were extracted from the phase signal[4]. ROIs were delineated in a straight part of the left and right femoral arteries. The time curves of all voxels in these ROIs were averaged. Possible phase drift was corrected by defining a reference region in fat tissue close to the artery[5]. The curve was characterized by the area under the curve (AUC300), the peak height and the full width at half maximum (FWHM). A paired Student T-test ($p \leq 0.05$) was used to test for significant differences in AIF characteristics of the two exams.

Results: The average AIF characteristics of test-retest data were 363.62±113.54mMs for AUC300, 7.76±1.57mM for peak height and 8.34±2.69s for FWHM. Characteristics between AIFs of two measurements were not significantly different: 23±33% for AUC300, 13±11% for peak height and 18±15% for FWHM. Similar relative differences were found for 7.5s and 10s group which were not significantly different from the 5s group: AUC300 19±21% and 33±54%; peak height 7±15% and 30±16%; in FWHM 8±19% and 35±23%. Significant differences however, were found for overall injection times larger than 10 seconds: lower peak height for 20s group (52±23%) and 30s group (100±16%) and larger FWHM for 15s group (44±39%), 20s group (72±33%) and 30s group (99±22%). No significant differences were found for the AUC300.

Discussion: Overall injection times less than 15s resulted in AIFs which have a lower and broader peak compared to the 5s protocol. DCE-MRI protocols with a prolonged injection time of more than 10s could result in lower reproducibility of the AIF.

[1] Verma et al, AJR 2012, [2] van Aerts et al, MRM 2008, [3] Lavini et al., MRM 2015, [4] Korporaal et al, MRM 2011, [5] Garpebring et al., 2011 Magma.

Acknowledgement: Dutch Cancer Society (NKI2013-5937) and DR THERAPAT project (FP7-ICT-2011-9, Project No. 600852).

TOWARDS MR-ONLY TREATMENT PLANNING- COMBINING UTE AND T1 WEIGHTED SPIN ECHO PULSE SEQUENCES; PHANTOM STUDY

Huan Yu, PhD, Sunnybrook Research Institute, Sunnybrook Health Sciences Centre
Ali Fatemi, PhD, Medical Physics, Sunnybrook Odette Cancer Centre
Arjun Sahgal M.D., Associate Professor of Radiation Oncology and Surgery, University of Toronto, Clinician Scientist, Sunnybrook Research Institute, Affiliate Scientist- Toronto
Western Research Institute , Radiation Oncology, Sunnybrook Odette Cancer Centre

Introduction and Purpose: Ultra-short Echo Time (UTE) sequence has shown potential to generate pseudo CT images due to its ability to differentiate cortical bone and air which are indistinguishable in common T1 and T2 weighted images. However, UTE is subject to weak bone signals, intensity non-uniformity and geometrical distortion. This study investigated a new approach in generating pseudo CT images by using the combination of our optimized UTE and T1 weighted spin echo pulse sequences which has high image quality and geometrical fidelity to delineate air, bone and water (soft tissues) comparable with CT.

Methods and Materials: A gel phantom containing chicken bones, ping pang balls filled with distilled water and air bubbles, was made. It scanned with MRI using our modified UTE and 2D T1W SE pulse sequences with (in plane resolution= 0.53mm, slice thickness= 2 mm) and CT with (in plane resolution= 0.5 mm and slice thickness= 0.75mm) as a ground truth for geometrical accuracy. In order to minimize geometrical distortion and intensity non-uniformity we were optimizing the UTE signal (echo times) based on T2 and subsequently fill out the kspace in Cartesian (classic) manner rather than radial. The UTE and T1W SE images were registered with CT using mutual information registration algorithm provided by Philips Pinnacle treatment planning system. The phantom boundaries were detected using Canny edge detection algorithm which identifies local maximum gradients of edges for CT, and MR images. The bone, air bubbles and water in ping pong balls were segmented from CT images using threshold 200HU, -400HU and from 0HU to 50HU, respectively. These tissue inserts were automatically segmented from combined UTE and T1W SE images using edge detection and relative intensity histograms of the phantom. The obtained segmentations of air, bone and water inserts were evaluated with those obtained from CT.

Results: Cortical bone, water and air can be clearly differentiated in our modified UTE images comparable to CT. Air and Spongy bone can be clearly shown in T1W-SE images. However, Water enclosed in ping pang balls and phantom materials are indistinguishable in CT and T1W-SE images. By combining UTE and T1W-SE images, the chicken bone, air and water enclosed in ping pang balls were successfully segmented. The maximum segmentation differences from combined MRI images (UTE and T1W SE) and CT are within 1.3 mm, 1.1mm for bone, air, respectively. The geometric distortion of UTE sequence is small less than 1 pixel (0.53 mm) of MR image resolution.

Conclusions and Discussion: Combining UTE and T1W-SE can utilize advantages of both imaging sequences which are ability to differentiate cortical bone and air with high contrast resolution, less intensity non uniformity and less geometrical distortion. Although, further investigation has to be made to make our UTE acquisition fast, and be able to suppress fat and/or long T2 components. Our approach indicates that MRI can be used solely for treatment planning and its quality is comparable with CT.

DOES PROSTATE RADIOTHERAPY TREATMENT PLANNING BENEFIT FROM MRI?*

Niina Rintelä, Eva Onjukka, Enrique Castellanos, Ingmar Lax, Milos Djordjevic
Karolinska University Hospital, Section of Radiotherapy Physics and Engineering, Dept. of Medical Physics

Introduction and purpose: MRI has been used to define target and risk organs for patients with implanted gold seeds (Gold anchor, Naslund Medical, Sweden) in the prostate at Karolinska University Hospital since December 2013. A CT image is also required for treatment planning and DRR generation and therefore the CT and MR images need to be co-registered. The aim of this retrospective study is to investigate how much the margin between the CTV and PTV needs to be extended due to the registration uncertainty, and the effect of this margin extension on the dose in the organs-at-risk (OAR). Another aim is to see if there is a benefit of using MR images for target definition in prostate radiotherapy by comparing PTV volumes based on CT-delineated CTV and MR-delineated CTV, respectively (using relevant margins).

Methods: A registration uncertainty was calculated from multiple registrations for 40 patients. The registrations were made on 3-4 gold fiducials with the rigid registration tool in Eclipse (Varian, USA). Variations between operators were studied and the results were incorporated in the calculation of the registration uncertainty. A simulation was made to determine the necessary extension of the PTV margin, given the registration uncertainty found in the registration study. Volumes of prostates delineated in CT and MR were compared to see if the general consensus that prostate delineated on MR is smaller than when delineated on CT applies to our data. VMAT plans were made in RayStation (Raysearch, Sweden) using multi-criteria optimization for patients with target and OARs delineated in CT (5 mm PTV margin) contra MR (extended PTV margin).

Results: Taking into account the variations between the operators, the registration uncertainty presented from this study was 1.4 mm. The simulation results indicated the PTV margin needs to be extended by at least 1 mm for adequate dose coverage of the CTV, to compensate for this uncertainty. The mean volume of the MR-based PTV, with a 6 mm margin, was significantly larger than the CT-based PTV (5 mm margin). The mean volume of the CTV delineated on MR and CT were equal. However, there was no significant difference in the NTCP of the rectum or bladder, if using a registered MR image for target and OAR delineation to a CT only planning process.

Conclusions: Due to the significantly larger volume that is treated when using registered MR/CT images for treatment planning, prostate patients may not benefit from routine MR imaging. However, the MR images could play a crucial role when training prostate segmentation.

DOSIMETRIC COMMISSIONING OF A HYBRID MRI RADIOTHERAPY SYSTEM

J.W.H. Wolthaus, K. Smit, B. van Asselen, A.C. Houweling, H.M. van Zijp, S.J. Woodings, S.S. Hackett, J.H.W. de Vries, J.G.M. Kok, J.J.W. Lagendijk, B.W. Raaymakers
University Medical Center Utrecht

Purpose: Three different hybrid MRI radiotherapy systems are becoming operational, for all, the dose is delivered in the presence of a magnetic field. This affects the dose distribution and radiation detectors used. The presented work addresses different dosimetric aspects of the commissioning of such hybrid systems.

Methods: The impact of the magnetic field has been quantified for an ionization chamber (NE2571) using the NCS18 (comparable to TG-51) reference dosimetry protocol. Also relative dosimetry by water tank and scanning ionization chambers, and 2D detectors arrays (PTW STARCHECK, Sun Nuclear IC PROFILER) as well as patient QA systems (Sun Nuclear ArcCheck, Scandidos Delta4) has been investigated. Furthermore, beam data collection and automated beam modeling is presented. A 3D measured dose map is reconstructed from measured dose profiles/images as input of the automated beam modeling. The tool was tested against dose maps from a TPS before obtaining the beam model parameters from the measured data.

Results: The NCS18 protocol can be used with the addition of a magnetic field correction factor (~2% for 1.5 T). Water tank measurements can be done with a modified water tank and the evaluated scanning ionization chambers performance is not affected by the magnetic field. The impact on detector arrays as well for patient QA systems was measurable, but implied hardly any consequences for relative dosimetry. Automated beam modeling using 3D dose maps yielded similar results as the manual modeling.

Conclusion: The magnetic field affects standard dosimetry protocols for QA and commissioning. Because the effect is deterministic, standard protocols can be adapted to allow the same QA tests as for conventional systems.

CHANGES IN LUNG CANCER DURING RADIOTHERAPY: AN ASSESSMENT OF FUNCTION AND MOTION ON 3T MRI

Shivani Kumar[1,2,3,] Gary Liney[3,1,2,5], Daniel Moses[6,7], Minghao Teo[4], Tony Young[4,2,3], Lois Holloway[2,1,3,4,5] Shalini Vinod[1,2]

(1) South Western Clinical School, School of Medicine, The University of New South Wales, NSW, Australia
(2) Liverpool and Macarthur Cancer Therapy Centre, NSW, Australia
(3) Ingham Institute of Applied Medical Research, NSW, Australia
(4) Institute of Medical Physics, University of Sydney, NSW, Australia
(5) Centre for Medical Radiation Physics, University of Wollongong, NSW, Australia,
(6) The University of New South Wales, Sydney, NSW, Australia
(7) Department of Radiology, Prince of Wales Hospital, NSW, Australia

Purpose: The purpose of this study is to investigate the use of MRI in assessing functional and motion changes in lung cancer during a course of curative intent radiotherapy.

Methods: Four patients with non-small cell lung cancer underwent MRI scans on a 3T Siemens Skyra scanner prior to treatment and on days 1, 11 and 21 during their treatment. For motion analysis free breathing TrueFisp scans were acquired, using a cardiac specific shim placed over the heart, in a single 4 mm plane in both the sagittal and coronal directions through the centre of tumour volume. A total of 30 frames were acquired which captured on average 21 breathing cycles with 0.7 x 0.7 mm resolution and TE/TR = 1.4/417-624 ms. Diffusion weighted imaging was acquired using an EPI sequence, in the axial plane, using a slice thickness of 4mm and b values of 0, 250, 500 and 750 s mm-2. Maximum tumour excursion was recorded together with area and diaphragm position. Manual analysis was based on tumour edge delineation at inspiration and expiration. Additionally semi-automated analysis of tumour and diaphragm motion was performed using in-house software (MATLAB), previously validated with phantom data. ADC maps were produced using vendor software and transferred off-line for further analysis. The tumour was then segmented by a thoracic radiologist, using the Haste T2 weighted images for reference and ADC histograms were calculated for segmented volumes using additional software.

Results: Tumour motion amplitude varied during treatment from the baseline measurement in all cases, with an average variation of 0.6 cm in tumour amplitude in cranio caudal direction. Amplitude of tumour motion did not match diaphragm motion range. There was up to 50% change in tumour cross section during the scans reflecting tumour motion out of plane. The mean ADC value of all tumours stayed constant or decreased slightly between the baseline and day 1. The mean ADC value of the tumours increased between day 1 and day 11 by approximately 0.2 x10-3 mm2s-1. Histogram analysis showed the percentage of voxels with moderately low ADC (i.e. < 1.0 x10-3 mm2s-1) increased between day 0 and day 1 and then decreased progressively from day 1 to day 21 in all cases.

Discussion: For this small cohort of patient's variation in motion and diffusion was shown over the course of RT. Diffusion changes were similar for all patients with a marked increases in ADC later in the course of treatment. Histograms rather than mean ADC value is a promising approach for ADC analysis. Tumour motion varied during treatment and did not correlate well with the diaphragm, highlighting the importance of direct tumour tracking, rather than correlation of tumour motion to surrogate motion.

DEVELOPMENT OF MULTI-PARAMETRIC MRI PROTOCOLS FOR PROSTATE FOCAL RADIOTHERAPY USING BIOLOGICAL OPTIMIZATION

Mary E Finnegan[1,2], Hayley M Reynolds[1,3], Gary Liney[4], Scott Williams[5], Bimal Parameswaran[5], Parisa Rahnema[1], Yu Sun[1], Darren Wraith[6], Annette Haworth[1,3]

(1) Department of Physical Sciences, Peter MacCallum Cancer Centre, Melbourne, VIC, Australia
(2) School of Applied Sciences, RMIT University, Melbourne, VIC, Australia
(3) Sir Peter MacCallum Department of Oncology, University of Melbourne, Melbourne, VIC, Australia
(4) Ingham Institute for Applied Medical Research, Liverpool Hospital, NSW, Australia
(5) Division of Radiation Oncology and Cancer Imaging, Peter MacCallum Cancer Centre, Melbourne, VIC, Australia
(6) Institute of Health Biomedical Innovation, Queensland University of Technology, QLD, Australia

Purpose: We present multi-parametric MRI (mp-MRI) protocols and initial results from an investigation into the relationship between prostate mp-MRI and histopathology. The ultimate aim is to use mp-MRI to inform our recently validated radiobiological model [1] which takes into account prostate tumour location and tumour characteristics, in order to plan optimal dose distributions for focal radiotherapy.

Methods: Patients with biopsy confirmed prostate cancer and scheduled for radical prostatectomy were imaged with a 3T Siemens Trio Tim scanner and torso surface coil. The mp-MRI protocol was adapted from standard clinical protocol based on the ESUR guidelines [2] to include measurements associated with tumour properties such as tumour location, cell density and Gleason Score. The imaging and post-processing protocols included 2D and 3D T2w imaging, DWI and ADC map calculation and DCE-MRI followed by pharmacokinetic parameter calculation. Additionally, a multiple gradient echo sequence was used to map R2* which has been previously associated with tumour hypoxia [3]. Building on methods developed by Park et al [4], we co-registered in vivo mp-MRI with 'ground truth' histology data using ex vivo MRI as an intermediate registration step. The ex vivo MR images were obtained the day after surgery with the formalin fixed prostate specimen placed in a custom designed sectioning box, which enabled histology sections to be cut in the same orientation as the ex vivo MRI slices.

Results: The mp-MRI protocol for quantitative parameter calculation for the prostate has been optimised to comply with clinical requirements and an appropriate scan time of 45 minutes. We obtained 3D T2w scans with 0.8 mm isotropic voxels in both the in vivo mp-MRI and ex vivo protocol, which enabled successful alignment of the images using deformable image registration (DIR). The 3D T2w scan was optimised to ensure high SNR for DIR and to give sufficient resolution for feature points and zonal regions to be identified by a radiologist and radiation oncologist for registration validation. Calculated R2* maps from initial data sets show values consistent with the literature (3) and registered mp-MRI and histology data have been examined using logistic regression and random forests with promising results for predicting tumour location and characteristics at a voxel level.

Conclusion: Our imaging protocol and registration methodology can be used to investigate the ability of mp-MRI to determine tumour location and characteristics. Machine learning methods are currently being developed to quantify the relationship of signals in our co-registered mp-MRI and histology data.

[1] Haworth, A., et al. (2013). "Validation of a radiobiological model for low-dose-rate prostate boost focal therapy treatment planning." Brachytherapy 12(6): 628-636.
[2] Barentsz, J. O., et al. (2012). "ESUR prostate MR guidelines 2012." Eur Radiol 22(4): 746-757.
[3] Hoskin, P. J., et al. (2007). "Hypoxia in Prostate Cancer: Correlation of BOLD-MRI With Pimonidazole Im munohistochemistry—Initial Observations." Int J Radiat Oncol Biol Phys 68(4): 1065-1071.
[4] H. Park et al., "Registration Methodology for Histological Sections and In Vivo Imaging of Human Prostate," Acad Radiol 15(8), 1027–1039 (2008).

FEASIBILITY OF REGISTERING MULTI-BAND CINE MR IMAGES TO VOLUMETRIC MORPHOLOGICAL IMAGES FOR MRI-GRT

Eric Paulson, Nikolai Mickevicius, Fabienne Lathuiliere, Martin Lachaine
Radiation Oncology, Radiology, Biophysics, Medical College of Wisconsin, Milwaukee, Wisconsin, United States
Elekta Instruments, AB

Purpose: Multi-band excitation accelerates MR image acquisition in the slice-select direction by simultaneously exciting a short comb of slices. Aside from an improvement in temporal resolution, the larger number of slices is hypothesized to improve the robustness of dynamic image registration and segmentation algorithms used in MRI-gRT. However, incomplete separation of simultaneously excited slices during reconstruction may adversely affect image registration accuracy. The goal of this work was to explore the feasibility of registering multi-band cine MR images acquired for intrafraction motion monitoring to volumetric images acquired for position verification.

Methods: Three-band SPGR and bSSFP radial CAIPIRINHA (CAIPI) images were acquired in the abdomen of one healthy volunteer on a Siemens 3T scanner using a sequence of our own design. A breath held 3D T1 VIBE sequence was acquired to mimic images acquired for daily position verification on an MRI-gRT system. The radial CAIPI images were reconstructed offline in Matlab. Image registration was performed by resampling the three separated multi-band radial CAIPI slices into a 3D volume and then registering the 3D T1 VIBE images using mutual information with a trust region gradient optimizer. Image registration results were verified using checkerboard images.

Results: The 3D T1 VIBE images were successfully registered to the bSSFP and SPGR radial CAIPI images, indicating that radial CAIPI is effective at separating aliased multi-band slices for image registration. Even with dissimilar contrasts, the bSSFP images were successfully registered with small variations in translations compared to SPGR images (2.42, -1.73, and -0.08 mm, versus 3.48, -1.05, and 0.48 mm, respectively, in x,y, and z directions for the bSSFP and SPGR radial CAIPI images).

Conclusions: Registration of multi-band radial CAIPI images acquired for intrafraction motion monitoring to volumetric images acquired for position verification on MRI-gRT systems is feasible. Future work will explore image registration and segmentation of multi-band radial CAIPI images for dynamic MLC tracking.

EVALUATION OF DIFFERENT APPROACHES TO OBTAIN SYNTHETIC CT IMAGES FOR A MRI-ONLY RADIOTHERAPY WORKFLOW*

Filipa Guerreiro [1], Jamie McClelland[2], Alex Dunlop[3], Ninon Burgos[2], M. Jorge Cardoso[2], Kee Wong[3], Simeon Nill[1], Uwe Oelfke[1], Antje-Christin Knopf[1]

(1) Institute of Cancer Research, London
(2) University College London
(3) Royal Marsden Hospital, London

Purpose: The gold standard for radiotherapy treatment planning is CT imaging, as it provides high spatial resolution and electron density values. The main arguments for substituting CT for MRI are the superior soft-tissue contrast of MR images and the avoidance of imaging dose. The establishment of a MRI-only workflow in RTP depends on the ability to generate a synthetic CT (sCT) that can be used for dose calculations and the ability to delineate accurate VOIs for treatment planning. In this study, we evaluate Bulk Density Assignment (sCTbda) and Atlas-based (sCTa) methods to generate sCTs for head and neck (H&N) patients.

Methods: sCTbda and sCTa based on T2_weighted MRI- and CT-scans acquired on the same day were generated for six H&N patients. For sCTbda, densities of 1.53 g/cm3 for bone and 0.001 g/cm3 for air were assigned to segmented structures in the MRI using a combination of threshold-based and manual delineation. The remaining anatomy was defined to be of water equivalent density. sCTa were obtained from an anatomical atlas based on seventeen pre-acquired pairs of non-rigidly aligned T2 MR and CT images. Local similarity measures (like local normalised correlation coefficient) were used to match the patient's MRI with the atlas database. Clinical VMAT plans with a prescribed dose of 65Gy were re-calculated on both sCTbda and sCTa. A dosimetric evaluation, including dose differences and gamma analysis, was performed using the original planning contours. Original contours and delineations/segmentations on the MRI and sCTa were evaluated in terms of shape, position and volume using the Dice Similarity Coefficient (DSC).

Results: Gamma analysis (2mm_2%) showed that dose distributions re-calculated on the sCTbda and sCTa were comparable. Compared to the original dose distribution, differences were less than 1Gy in the PTV. Differences of Dmean in the PTV ranged from -0.9% to 0.3% for sCTbda and from -0.4% to 0.4% for sCTa. More points at the outer contour failed the gamma criteria due to external contour differences.The outlines of the body and bone contours in the sCTa and the original CT were very similar in shape, position and volume. Obvious deviations in shape and in volume could be observed between original bone contours and contours based on the MRI. However, DSC values ranged from 0.73 to 0.86 when comparing bone contours on the sCTa with the original CT, and from 0.71 to 0.82 when comparing bone contours on the MRI with the original CT.

Conclusions: Dose re-calculations on sCTbda and sCTa showed no clinically relevant dose differences to the original dose distribution on the planning CT. Hence, sCT obtained with either method are suitable to perform dose calculations. Also, contours based on MRI and sCTa were found to be similar. However, segmentation of bone on the MRI cannot be performed fully automatically and the sCTa cannot provide information of the target volume. We therefore suggest combining soft tissue contours based on MRI with bone contours obtained from the sCTa in order to establish a MRI-only workflow for future MR-Linac machines.

UTE: ITS POTENTIAL ROLE AS A DEDICATED RADIOTHERAPY PLANNING TECHNIQUE.

GP Liney[1-4], R Rai1, B Schmitt[7], D Grodzki[8], J Dowling[6], L Holloway[1-5], P Metcalfe[4].

(1) Ingham Institute of Applied Medical Research, NSW, Australia
(2) Liverpool and Macarthur Cancer Therapy Centre, NSW, Australia,
(3) The University of New South Wales, Sydney, NSW, Australia,
(4) Centre for Medical Radiation Physics, University of Wollongong, NSW, Australia,
(5) Institute of Medical Physics, University of Sydney, NSW, Australia
(6) CSIRO, Brisbane, QLD, Australia
(7) Healthcare sector, Siemens Ltd Australia, NSW, Australia
(8) Healthcare sector, Siemens AG, Germany

Introduction: Ultra short echo time (UTE) sequences are able to achieve the shortest possible TE limited only by transmit/receive switching times and gradient slew rates and requiring no hardware upgrades. These have the potential to generate signal in previously invisible structures and reduce susceptibility artefacts which could have advantages for radiotherapy (RT) planning including: i) better cortical bone segmentation, ii) improved accuracy of implantable markers and iii) direct imaging of beam attenuating materials. The purpose of this study was to explore the potential applications of UTE sequences in the context of RT on our MR-Simulator and with regard to our future MR-Linac development.

Methods: All imaging was performed on a 3.0 Tesla wide bore Siemens Skyra system located in the cancer therapy centre. Two works-in-progress prototype sequences ('UTE' and 'PETRA') were evaluated using several phantoms imaged over a range of ultra short TEs (40 μs to 1 ms) as well as routine sequences. Firstly, a quality assurance test object was constructed to evaluate image quality which consisted of material expected to produce rapidly decaying signal: NiCl2 solution, gadoteric acid and adhesive putty. Secondly, a porcine specimen was imaged using a 20 channel head & neck coil to examine the appearance of cortical bone and develop post processing techniques for improved bone segmentation. Thirdly, to examine signal generation in RT relevant materials two further tests were performed; vinyl-plastic bolus (superflab, NL-TEC) was wrapped around a water phantom and imaged in the integrated body coil to simulate low SNR of the MR-Linac. This phantom was then imaged on its own using a 4 channel flexible coil with a FOV extended to include this coil. Finally, UTE sequences were compared against our standard prostate seed visualisation protocol (FLASH, high bandwidth, TE = 4 ms) in a gel phantom containing three gold and three non-metallic implantable markers (Polymark, NL-TEC).

Results: PETRA generally demonstrated superior image quality although at the lowest achievable TE artefacts were observed in the PETRA sequence but not the standard UTE sequence. In the porcine specimen structures of periosteum, endosteum and cortical bone (SNR = 38) were all visible. However, fat suppression was found to be non uniform and not useful. The use of two echoes allowed air, bone, fat and water to be separated. Plastic bolus was invisible on standard sequences but could be seen as TE was reduced below 10 ms with SNR increasing from 6.5 to 30.0 with UTE. The RF coil was successfully segmented from the image with SNR > 13. Artefacts from the fiducial markers were significantly reduced by a factor of 16.

Discussion: We have demonstrated several benefits of UTE sequences for use in current and future RT practice which may make this the sequence of choice for RT planning. These include bone segmentation and accurate MR-compatible marker localisation. These sequences also aid in the direct visualisation of plastic materials- including bolus, which may be required to reduce skin dose for an 'in-line' MR-Linac, and the RF coil- to permit attenuation correction of these structures.

SURFACE DOSE OUTSIDE THE PRIMARY RADIATION FIELD OF A TRANSVERSE MR-LINAC

S.L. Hackett, B. van Asselen, J.W.H. Wolthaus, S.P.M. Crijns, J.G.M. Kok, J.J.W. Lagendijk,
K. Ishakoglu, B.W. Raaymakers
University Medical Center Utrecht

Introduction: The magnetic field of the MR-linac deflects the trajectories of electrons and therefore alters the radiation dose distribution, particularly at the surfaces of tissue-air interfaces. The magnetic field also changes the trajectories of contaminant electrons. A transverse magnetic field causes dose from contaminant electrons to be deposited in tissues outside the primary radiation field. We have measured the dose distributions outside the primary radiation field in an MR linac with a transverse magnetic field to assess the contribution from contaminant electrons.

Methods and materials: Doses were measured with Gafchromic EBT2 films (ISP, Wayne, USA) covered by 0, 1, 2, 3, 4 or 5 mm of solid water, with 5 cm of solid water for backscatter. The films were 15 x 15 cm2 and the slabs were 29.8 x 29.8 cm2. The radiation field was 10 x 10 cm2 at the isocentre, and the phantom was positioned in the x-z plane (IEC fixed co-ordinate system). The surface film was positioned outside the radiation field at y = -10 cm (position 1), ie. 5 cm from the beam edge at the level of the isocentre. The B0 magnetic field was parallel to the y-axis and the gantry angle was set to 0°. Measurements were repeated with the films in the y-z plane and the surface film at x = -10 cm (position 2) to quantify the dose from scattered and leakage radiation.

Films were exposed with 2000 MU, equivalent to a maximum dose on beam central axis, Dmax, of 20 Gy. Doses were interpolated from calibration curves of optical density to dose from 100 kVp and a 6 MV photon beam.

Results: The dose distribution to the surface film at position 1 showed a clearly higher dose in the region parallel to the divergent x-ray beam, with a full-width half maximum value of 9.6 cm at the level of the isocentre. However, the surface dose distribution at position 2 was comparatively uniform, as were the dose distributions to all films at depths of at least 1 mm. The electron dose was estimated by subtracting the optical density distribution of the film at position 2 from that of the film at position 1, and converting the optical density to dose using the 100 kVp calibration curve. All other films were converted using the 6 MV calibration curve. The total surface dose at position 1 at the level of the isocentre was 5.2% of Dmax, comprising a dose of 2.7% from photons and 2.5% from electrons. The doses to all other films were all less than 2.3% of Dmax at the level of the isocentre.

Discussion and conclusions: The surface dose from low-energy electrons generated in air is 2.5% of the Dmax dose at a point 5 cm from the edge of a 10 x 10 cm2 field. However, 1 mm of solid water is sufficient to absorb these electrons and reduce the dose from 5.2% to less than 2.3% of Dmax.

ASSESSING SALIVARY GLAND FUNCTION USING DIFFUSION WEIGHTED MAGNETIC RESONANCE IMAGING TO IMPROVE RADIOTHERAPY INDUCED XEROSTOMIA

Mr Jonathan Wyatt, Dr Hazel McCallum, Dr Rachel Pearson, Mr James Snell, Mrs Jill McKenna,
Professor Andrew Blamire, Dr Charles Kelly
Newcastle upon Tyne Hospitals NHS Foundation Trust

Introduction: Xerostomia is a major complication from head and neck radiotherapy due to radiation damage of the salivary glands. Gland sparing is possible with intensity modulated radiotherapy but which gland should be spared? This study will investigate the utility of lemon juice Stimulated Diffusion Weighted Magnetic Resonance Imaging (SDW MRI) to determine salivary gland function and so inform the choice of gland sparing.

Methods: This is a two-stage feasibility study. During stage one 10 healthy volunteers will undergo SDW MRI with a 1.5T Siemens Magnetom Espree. The Apparent Diffusion Coefficient (ADC) and stimulation-induced change in ADC will be measured using the scanner software. The volunteers will also complete a xerostomia questionnaire. During stage two 15 recruited head and neck patients will have SDW MRI scans incorporated into their routine planning MRI scan and complete a xerostomia questionnaire. Four weeks after radiotherapy the patient will have another SDW MRI scan and questionnaire. The dose to the salivary glands will be determined from the patient's treatment plan using Oncentra (Nucleotron, Elekta).

Outcomes: Stage one will determine the optimum acquisition set-up and intra- and inter-subject reproducibility of SDW MRI. This is essential for SDW MRI to be used to determine relative gland function. Stage one will also determine the correlation of measured gland function with xerostomia questionnaire score. Stage two will assess the correlation of change in gland function to change in xerostomia score and to mean dose to the salivary gland.

Discussion: Choosing to spare the better functioning gland will potentially reduce xerostomia. SDW MRI potentially provides a quick and non-invasive method of determining the better functioning gland. This study will determine the utility of SDW MRI for radiotherapy treatment planning.

COMPARISON OF MRI AND CT-DERIVED WHOLE BREAST RADIOTHERAPY TARGET VOLUME CONFORMITY

Elise M. Pogson, Geoff Delaney, Verity Ahern, Miriam Boxer, Christine Chan, Steven David, Marion Dimigen, Jennifer A. Harvey, Eng-Siew Koh, Karen Lim, George Papadatos, Mei Yap, Vikneswary Batumalai, Elizabeth Lazarus, Jesmin Shafiq, Gary Liney, Catherine Moran, Peter Metcalfe, Lois Holloway
Liverpool Hospital and the Ingham Institute of Applied Medical Research

Introduction: This study aims to compare Magnetic Resonance Imaging (MRI) to Computed Tomography (CT) imaging modalities for contouring of breast radiotherapy treatment volumes in the supine treatment position. The study aims to investigate if MRI contributes additional benefit to contour conformity, due to its better soft tissue contrast, or if MRI is comparable to CT.

Methods: Both a 3T scan of T2-weighted MRI spin echo sequence with 2mm slice thickness and 1.707px/mm resolution and a standard radiotherapy CT scan at 1.024px/mm resolution were undertaken for 10 breast cancer patients with identical supine radiotherapy set-ups, taken a few hours apart. The T2 sequence was selected by using a trial of healthy volunteer images of non-contrast T1 and T2 sequences which were assessed by a team of four Radiation Oncologists and two Radiologists to establish the best image for radiotherapy purposes. 11 observers (2 Radiologists and 9 Radiation Oncologists), across 4 different hospitals, contoured both the MRI and CT datasets. Prior to the study a trial data-set of one MRI and matching CT were sent out for pre-voluming education and contouring protocol revision. Following this for all datasets both a whole breast volume and a seroma volume were contoured. A STAPLE volume was generated for each dataset from all contours to provide a gold standard volume which was compared with all individual observer contours to generate Dice similarity coefficients. The kappa statistic for each of these data-sets was also determined.

Results: The average (± the 95% confidence limit) over all 10 patients and 11 observers for the whole breast Clinical Target Volume (CTV) kappa statistic for CT and MRI was 0.802±0.022 and 0.804±0.019 respectively. This is in the near perfect category for the kappa statistic. The Seroma volume had much lower agreement (in the fair agreement range) of 0.32±0.12 and 0.32±0.13 for CT and MRI respectively. The average Dice similarity coefficient for all 10 patients over all 11 observers was 0.8836 with a variance of 0.0037. Similarly the MRI's average CTV Dice similarity coefficient was 0.8867 with a variance of 0.0023. There was no statistically significant difference between the CT and MRI's CTV conformity ($p>0.05$). MRI CTV volumes (of average 539±34cc) were consistently smaller than the CT (of average 571±31cc) ($p<0.05$).

Conclusions: No measureable difference between contour conformity was seen between MRI and CT for supine whole breast and seroma volumes. MRI is comparable to CT for contour conformity and could be utilised in an MRI-only setting such as adaptive radiotherapy within an MRI-Linac possibly to account for breathing motion. Increased numbers of patients are needed to confirm these results. Other limitations of this study include the relative inexperience of the observers with MRI-based contouring compared to CT in breast radiotherapy. Further experience and training in MRI for breast radiotherapy volumes is needed to fully determine if there is additional benefit in from utilising MRI in radiotherapy target volumes. Other MRI sequences that use contrast may also increase contour conformity.

RADIATION-TRANSPARENT 1.5T MR-LINAC RECEIVE COIL SOLUTION FOR PELVIS AND ABDOMEN

Wycliffe Raduma[1], Panu Vesanen[1], Tiina Näsi[1], Teemu Niemi[1], Joel Tulppo[1], Martin Deppe[1], Juha Oila[1], Tero Virta[1], Annemaria Halkola[1], Jukka Tanttu[1], Johan Overweg[2], Jarmo Ruohonen[1]

(1) Philips Healthcare, MR Therapy, Vantaa, Finland
(2) Philips Research Laboratories, Hamburg, Germany

Introduction: The magnetic resonance (MR) subsystem of an integrated MR-Linac system produces images of the anatomy before, during, and after radiotherapy (RT) treatment to aid in target localization, treatment adaptation, and for assessing treatment response. The images are acquired with radiofrequency (RF) receive coils to which the MR-Linac poses additional requirements as compared to diagnostic MR imaging, such as insensitivity to radiation, low and uniform attenuation of the radiation beam, and intact body outline. This abstract describes results of volunteer and phantom studies with a new coil solution optimized for imaging the torso on a 1.5T MR-Linac system.

Methods: Measurements were performed on an industry-built 1.5T MR-Linac that is designed to avoid interference between Linac and MR subsystems and to minimize radiation beam attenuation. The Linac rotates on a circular gantry around the central part of the MR subsystem through which the radiation beam can pass. The gantry was static during measurements presented in this work; volunteers were imaged without active Linac components installed.
The coil solution constitutes a combination of anterior and posterior coils. The anterior coil is placed on top of the patient and indexed and fixed relative to the patient table with a coil frame. When attached to the coil frame, the anterior coil does not deform the body outline. The posterior coil is located below the tabletop close to the patient and has a fixed position relative to the radiation window. Both coils have four parallel channels, allowing a maximum theoretical SENSE factor of 4 in right-left direction and 2 in anterior-posterior direction. A key feature of the coils is freedom from structural inhomogeneity in the radiation window (22x58 cm2 in the isocenter) and minimal beam attenuation. The coil components have been tested to withstand the harsh radiation treatment environment. The pelvises of nine volunteers and abdomens of five volunteers were imaged with the developed coil solution on the MR-Linac using sequences envisaged suitable for RT planning (T2-weighted TSE, field-of-view 453x320x340 mm3, SENSE factor 3.2) and near-real time monitoring (balanced SSFP, SENSE factor 3, field-of-view 460x400 mm2, scan time 0.2 seconds/frame). For comparison, the volunteers were also imaged on a comparable diagnostic scanner (Philips Ingenia 1.5T) with commercial coils. In a separate experiment, phantom images were measured with and without simultaneous irradiation (approximately 6 Gy/min, beam size 22x25 cm2 in the isocenter).

Results: Visual inspection of the volunteer images showed that the coils provided adequate field of view coverage and SNR. The SNR of the images at MR-Linac (193±30) was comparable to Ingenia 1.5T (210±21) in the hip joints of the nine pelvis subjects. The coil frame allowed for acquiring images without deforming the skin contour. A SENSE factor of 3.6 was achievable. Phantom studies showed no differences in SNR during irradiation (156±4) as compared to without irradiation (154±4).

Conclusion: The introduced coil solution provides means to obtain high-quality MR images for RT treatment planning and near-real-time treatment monitoring while taking into account additional requirements posed by the Linac subsystem of the MR-Linac.

INVESTIGATION OF ADAPTING BRAIN GLIOMA PLANS FOR RIGID TRANSLATION IN A 1.5T MR-LINAC

M. Ruschin, Y. Lee, A. Kim, H. Soliman, A. Sahgal, B. Keller
Odette Cancer Centre

Purpose/background: An integrated 1.5T MRI with a linear accelerator (MRL) can be used for plan adaptation based on direct visualization of the disease and soft tissue, but the presence of the magnetic field may influence the quality of adapted plans if not accounted for. The purpose of the present study is to quantify changes in the dose distribution for the MRL when the original plan is adapted to account for translations for brain glioblastoma (GBM) patients.

Materials and Methods: Two left-sided GBM cases (Case1: 40Gy in 15; Case2: 60Gy in 30) treated with intensity modulated radiotherapy (IMRT) at our institution were re-planned using a MRL beam model in the treatment planning system (TPS) (Monaco, v5.09.06, Elekta Inc). The TPS incorporated the effects of the magnetic field using a Monte Carlo dose engine. The beam model and planning parameters selected were similar to the MRL system: MLC with 7mm thick leaves oriented cranial-caudal; backup jaws perpendicular to MLC motion; flattening filter free; step-and-shoot IMRT with 7 beams; and isocentre placed in the centre of the imaging volume. Each reference plan resembled its clinical counterpart in terms of target coverage and satisfied all clinical organ-at-risk (OAR) dose constraints. For each case, a 4mm lateral shift was simulated compared to reference. Three corrective adaptations were performed: the system's virtual couch shift (VCS) model only ("VCS-only"), segment weight optimization (VCS+SWO) and segment shape optimization (VCS+SWO+SSO). The adapted plans were normalized to have the same PTV receiving 95% of the prescription (V95) as the reference, and subsequently were compared to the reference plans in terms of PTV (D95, D50, and D2), and OARs (D50 and D2). For Case1, the process was repeated but with the magnetic field turned off in the TPS for the reference and all plan adaptations.

Results: For PTV, the largest differences occurred in Case2, where VCS-only had a 1.7% higher D2 than the reference plan: 6511cGy vs. 6402cGy. Qualitatively, the OAR DVHs exhibited larger variation between the adapted plans. The largest excursion was the optic nerve having 9% and 13% larger D50 in Case 1 and 2, respectively, using VCS-only compared to reference. For the VCS+SWO+SSO plan, the D50 and D2 for OARs on average decreased compared to reference for near identical PTV coverage. For Case1, when the process was repeated without the magnetic field, the same trends were observed as with magnetic field but with fewer total monitor units (410 vs. 933) and lower OAR doses in the VCS+SWO+SSO plan.

Conclusion: Adapted dose distributions using the MRL were investigated for a simulated 4mm rigid translation for GBM. Segment shape and weight optimization lowered OAR doses in adapted plans compared to reference or to aperture-shift only. Similar trends were found when the process was repeated with the magnetic field turned off, but further investigation is warranted, including quantifying dose-difference maps and simulating more conditions. The present study did not account for aspects related to deliverability or quality assurance.

UNCERTAINTIES IN HIGH-RISK CTV (HR-CTV) DELINEATION FOR CERVIX BRACHYTHERAPY: APPLICATION OF GEC-ESTRO GUIDELINES IN THE AUSTRALIAN & NEW ZEALAND SETTING

Shalini K. Vinod[1,10], Karen Lim[1,10], Lauren Bell[2] , Jacqueline Veera[3], Lucy Ohanessian[1], Ewa Juresic[1], Nira Borok[4], Philip Chan[5], Raphael Chee[6], Viet Do[7], Geetha Govindarajulu[8], Carol Johnson[9], Daniel Moses[10], Swetha Sridharan[8], Sylvia Van Dyk[11], Lois Holloway[1,12]

(1) Cancer Therapy Centre, Liverpool Hospital, NSW, Australia.
(2) Centre for Medical Radiation Physics, University of Wollongong, NSW, Australia.
(3) Peter MacCallum Cancer Centre, Bendigo, Victoria, Australia.
(4) Department of Radiology, Liverpool Hospital, NSW Australia.
(5) Department of Radiation Oncology, Royal Brisbane and Womens Hospital, Queensland, Australia.
(6) Genesis Cancer Care, Perth, Western Australia, Australia.
(7) Crown Princess Mary Cancer Centre, Westmead Hospital, NSW, Australia.
(8) Department of Radiation Oncology, Calvary Mater Hospital, Newcastle, NSW, Australia.
(9) Wellington Blood and Cancer Centre, Wellington Hospital, New Zealand.
(10) University of NSW, NSW, Australia.
(11) Peter MacCallum Cancer Centre, East Melbourne, Victoria, Australia.
(12) Ingham Institute of Applied Medical Research, Liverpool Hospital, NSW, Australia.

Introduction & Purpose: Since the publication of the GEC-ESTRO guidelines in 2005, image-based brachytherapy has been implemented throughout many Australian and New Zealand centres. However, only some radiation oncologists have attended the GEC-ESTRO image-based brachytherapy course and familiarity with contouring on MRI is variable. The aim of this study was to evaluate the interpretation of GEC-ESTRO guidelines for cervical cancer by measuring interobserver variability in HR-CTV delineation.

Methods & Materials: Seven radiation oncologists and two radiologists delineated HR-CTV on MRI datasets from 10 consecutive patients undergoing cervical brachytherapy at a single institution. The images were taken on a 3T MRI from the first or second fraction of brachytherapy. The participants were provided with a clinical history, diagnostic imaging results and clinical diagram of EUA findings at brachytherapy insertion. Two reference contours were created for comparison, a simultaneous truth and performance level estimation (STAPLE) contour and a CONSENSUS contour between two radiation oncologists and a radiologist. The agreement between observer contours and the STAPLE and CONSENSUS contours was assessed using the Dice Similarity Coefficient (DSC) and Mean Absolute Surface Distance (MASD).

Results: The DSC ranged from 0.60-0.86 with STAPLE reference and 0.47-0.81 with CONSENSUS reference. An acceptable DSC of >0.7 was achieved for 8/10 cases using the STAPLE reference and 7/10 cases using the CONSENSUS reference. The MASD ranged from 1.8mm-9.5mm with STAPLE reference and 1.7mm-11.7mm using the CONSENSUS reference. A mean MASD of <5mm was achieved in 8/10 cases using the STAPLE reference and 7/10 cases using the CONSENSUS reference. The greatest variability was seen in patients with T3b-T4 disease and in the superior-inferior direction.

Conclusions: GEC-ESTRO guidelines have been applied consistently in Australia and New Zealand with an acceptable range of variation in HR-CTV delineation. Further analysis will be performed to assess the dosimetric consequences of this.

A COMPARISON STUDY FOR US- AND MR-BASED DOSE PLANNING IN HIGH-DOSE-RATE INTERSTITIAL PROSTATE BRACHYTHERAPY*

Susanne Rylander, Department of Clinical Medicine, Aarhus University Hospital, Aarhus, Denmark
Simon Buus, Department of Oncology, Aarhus University Hospital, Aarhus, Denmark
Lise Bentzen, Department of Oncology, Aarhus University Hospital, Aarhus, Denmark
Kari Tanderup, Department of Clinical Medicine, Aarhus University Hospital, Aarhus, Denmark

Introduction and purpose: The supplementation of MR imaging in US-guided high-dose-rate (HDR) prostate brachytherapy (BT) has improved target delineation and applicator reconstruction due to superior soft-tissue contrast and needle visualization. The purpose was to compare dose planning for US- and MR-based HDR-BT in terms of prostate contouring, needle reconstruction and dose-volume parameters and to evaluate the dosimetric impact to target and organs at risk (OAR) caused by the contouring- and needle reconstruction uncertainties on US.

Material and Methods: US- and MR images were acquired post needle insertion for 20 BT fractions for 10 patients treated consecutively with combined EBRT and BT. Contouring of the prostate target (CTVP) and OARs, needle reconstruction and dose optimization were performed in OncentraProstate (v. 4.2, Elekta). Dose planning was performed independently on US (PlanUS) and MRI (PlanMR). Dose planning objectives were; CTVP D90%>100%=8.5 Gy, CTVP+3mm D90%>95% (Gy) (CTVP+3mm=CTVP plus a 3 mm margin, constrained to bladder and rectum), urethra V10Gy<3.5%, rectum D2cc <75%. Prostate contouring and needle visualization on MRI was considered as the gold standard. The dosimetric impact of the target contouring- and needle reconstruction uncertainties in the US plans was evaluated by performing a rigid US/MR registration followed by needle position corrections in x- and y-direction according to needle visualization on axial MRI. The planned dose distribution in PlanUS was not modified. The resulting target- and OAR dose, after needle correction (PlanUS corrected), was evaluated on MR prostate contours and US OAR contours, respectively.

Results The preliminary results are based on evaluations done on 10/20 consecutive BT fractions. The mean prostate volume was 31 ± 6 cm3 on US- and 30 ± 9 cm3 on MR images (p=0.5). The mean D90% to targets in PlanUS (CTVP=108 ± 6%; CTVP+3mm=96 ± 8%) were not significantly different from PlanMR (CTVP=106 ± 6%; CTVP+3mm=95 ± 7%) (p=0.1, p=0.3, respectively). However, the target dose in PlanUS corrected was lower, by a mean of 4 ± 6% (p=0.06) to CTVP and 6 ± 10% (p=0.07) to CTVP+3mm as compared to PlanUS . The mean D2cc rectum was reduced by 4 ± 10% (p=0.4) with PlanMR as compared to PlanUS and PlanUS corrected. The urethra volume receiving 10 Gy never exceeded 3.2% for PlanUS and PlanMR, but was significantly higher in PlanUS corrected by 13 ± 18% (p=0.02) as compared to PlanUS.

Conclusions: Prostate target volumes on US- and MR images were not significantly different and the planned target doses were comparable for the US- and MR plans. The MR plans achieved a lower rectal-dose as compared to US. After needle position corrections in the US plans, the resulting doses were lower to MR based targets and higher to urethra as compared to initially planned.

QUANTIFICATION OF GEOMETRIC ERRORS FOR MR-BASED RADIATION THERAPY PLANNING IN PROSTATE

Steffen Weiss[1], Christian Stehning[1], Aleksi Halkola[2]

(1) Philips Research Laboratories, Hamburg, Germany,
(2) Philips Healthcare, MR Therapy, Vantaa, Finland

Purpose: The purpose of this work is to quantify the contributions to MR-specific image distortions for a prostate mDIXON MRI sequence and to compare them to geometrical errors due to physiological motion. This is especially important for dose prescriptions based only on MRI without any CT image available for geometrical reference.

Methods: Residual distortions due to gradient non-linearity and B0 inhomogeneity after system corrections were measured in a clinical 1.5T Ingenia MR system (Philips Healthcare, Best) using a custom-made 3D distortion phantom consisting of a grid of beads (coverage: LR=550mm, AP=300mm, FH=455mm). A 3D-T1w-mDIXON sequence was used (resolution=$(1.7mm)^2$ x 2.5mm, PBW=1082Hz, Tacq=1min50s), which enables a segmentation of soft tissue, fat, air, and cortical and trabecular bone and subsequent calculation of attenuation maps [1]. An inversion of the readout direction was used to distinguish gradient non-linearity from off-resonance effects. Off-resonances in patients were measured using off-resonance maps (resolution $(2mm)^2$ x 3mm) in nine prostate patients, and respective shifts along the readout direction were calculated for the mDIXON sequence. Physiological motion due to respiration, coughing, peristaltic motion, and contraction of the pelvic floor was determined in eight volunteers using a dynamic 2D T2w-SSFP sequence in sagittal and coronal orientation (Tacq=392ms per frame, resolution $(1.6mm)^2$ x 10mm).

Results: The distortions due to gradient non-linearity in phantom were <0.5mm in the region usually covered by the prostate, <1 mm within a 400mm sphere, and reached 3mm at one corner of the phantom. The distortions due to off-resonances in phantom were <0.4mm in the prostate region, <1.4mm in a 400mm sphere, and reached 3mm at very few locations at the edges of the phantom. The distortions due to off-resonances in patients were <0.05mm within the prostate and <0.5mm in the entire scan volume. Prostate motion in volunteers due to peristaltic motion was negligible. Respiration-induced prostate motion was <1mm in average but reached up to 1.7mm in one volunteer. Respiration-induced abdominal wall motion was 2mm to 16mm. Coughing and voluntary pelvic floor contraction caused prostate motion of 3mm to 11mm and 3mm to 35mm, respectively. A remaining prostate shift of 3mm to 11mm was observed after performing these tasks.

Discussion and Conclusion: MRI-specific image distortions in patients may in the worst case add up to 0.6mm in the prostate and are mostly <1.5mm across the entire FOV of the mDIXON sequence. This is less than the typical error of 2mm in CT/MR image registration for the prostate [2]. Distortions are largest at the body outline, which is relevant for calculation of absorption of radiation and suggests further research on specific corrections. However, all MRI-specific distortions were found to be small when compared with motion during respiration, coughing, and pelvic floor contraction. While position deviations due to coughing and pelvic floor contraction are mostly transient, importantly, these also resulted in a large remaining shift of the prostate (3mm to 11mm), which is highly relevant for therapy.
[1] Helle et al. Proc. of 22nd ISMRM 2014;p4238. [2] Nyholm et al. Radiat Oncol 2009;4:54.

DOSIMETRIC INVESTIGATION OF MR-ONLY CO-60 TREATMENT PLANNING USING A COMMERCIAL SYSTEM FOR MR-IGRT

H. Omar Wooten, Sridhar Yaddanapudi, Lakshmi Santanam, Harold Li, and Sasa Mutic
Washington University in St. Louis

Purpose: All patients (>100) treated in our department using a cobalt-60 (Co-60) magnetic-resonance image guided radiation therapy (MR-IGRT) device received CT simulations, and most were also simulated on the MR-IGRT on the device immediately after CT simulation. During clinical treatment planning, the CT was used to determine relative electron density (RED) using a CT-to-RED calibration table and the MRI was registered as a secondary dataset for target delineation. However, since we have begun to use this device for online-adaptive radiotherapy, there is increasing interest to use MR dataset as the primary image for clinical planning. The purpose of this study is to determine whether the simulation CT is still a necessary component of treatment planning with this device, or whether planning can achieve similar results by applying bulk RED overrides, thereby significantly reducing the total simulation time required for each patient.

Methods: Four patients who received treatment using a commercial MR-IGRT device were selected for analysis (2 abdomen, 1 lung, and 1 pelvis) using plans and contours computed and derived on CT primary datasets. In this study, beams and CT-derived clinical contours were rigidly copied to MR datasets acquired during the patients' first treatment fraction with the simulation CT registered as a secondary dataset. Each plan was recomputed using CT-based RED, then re-optimized using combinations of default bulk RED overrides (water = 1.00, lung = 0.26, tissue = 1.02, and bone = 1.12): water/lung and tissue/lung for the lung patient, water/bone, tissue/bone, water only, and tissue only for the abdomen and pelvis patients). Additionally, each CT- and RED-overridden plan was re-optimized to include the effects of the static magnetic field. All plans were normalized to the same PTV coverage as the clinical plan. Three-dimensional dose-difference volumes and dose-difference DVHs were computed for bulk density override plans, and 3D gamma analyses between each plan and its accompanying magnetic field plan were performed using 3%/3 mm and 2%/2 mm dose difference and distance-to-agreement criteria. Gamma values were measured inside the PTV and Skin structures only.

Results: The average differences in PTV and organs-at-risk mean dose for all RED combinations relative to CT-computed plans were -0.19 Gy, and -0.34 Gy, respectively. The average PTV and Skin gamma pass rates for all RED combinations tested were 99.88% and 98.35% for 3%/3 mm criteria, and 96.1% and 94.2% for 2%/2 mm. No systematic differences in DVHs or isodoses were observed.

Conclusions: A commercial MR-IGRT system can produce high quality treatment plans with similar dosimetry as CT-derived dose distributions, but without the need for CT scans. Additional analyses are needed to identify for which patients MR-only simulation would provide sufficient target delineation in the absence of CT simulation.

THE ELECTRON RETURN EFFECT ON IMRT PLANS IN MR-GUIDED RADIOTHERAPY

Xinfeng Chen PhD, Phil Prior PhD, Guangpei Chen PhD, X. Allen Li PhD
Department of Radiation Oncology, Medical College of Wisconsin

Purpose: In an integrated MRI-guided radiation therapy (RT) delivery machine, such as the MR-Linac, the presence of transverse magnetic-field (TMF) inevitably results in the electron return effect (ERE) that perturbs the dose distribution, especially near tissue-air interfaces. The purpose of this study is to investigate the ERE on IMRT plans of common tumor sites with tissue-air or tissue-lung interfaces.

Methods: The step-&-shoot IMRT and VMAT plans for pancreas, lung, breast and head & neck (HN) cases, were generated following the commonly used does volume (DV) criteria. All cases selected include either air cavities or tissue-lung interfaces in the beam paths. In each case, three types of plans were generated: 1) the original plan generated without a TMF, 2) the recalculation plan with TMF =1.5 T based on the original plan (no optimization), and 3) the optimization plan generated with TMF=1.5T. A research planning system (Monaco, Elekta) with Monte Carlo dose engine capable of computing dose under TMF was used to generate the IMRT/VMAT plans. These three plans were compared based on a series of DV parameters including the V100% (volume covered by 100% prescription dose) and D95% (dose covering 95% of the volume) in the PTV. The DV parameters for a 1mm thick tissue around the air cavity/skin surface used were Dmax (Maximum dose) and D1cc (maximum dose to 1cc volume).

Results: The presence of the 1.5T TMF resulted in reduced V100% and D95% for PTV, but the difference are all less than 4%. The D1cc on the skin was increased considerably in all cases: 10% increase for breast, 20% for HN, 26% for lung and 33% for pancreas cancer cases. The dose change on air cavity walls were site dependent: 1% to 2% difference for HN and breast cancer, respectively; 7% difference for lung cancer; and 1% to 9% differences for pancreatic cancer depending on the location and the size of air cavities. The dose change on heart for both lung cancer and breast cancer is less than 4%. The dose change on left/right parotid glands is at most 2% for the HN case. The pancreas VMAT plan gives much smaller Dmax and D1cc on air-cavity wall a,nd skin compared to fixed-beam pancreas IMRT. When the TMF were considered in the plan optimization, the doses on air-cavity wall and skin were significantly reduced compared to the recalculation plans.

Conclusion: The ERE due to the presence of the TMF in MR-guided RT can significantly affect the dose distributions, particularly on tissue-air or tissue-lung interfaces. These changes can be substantially reduced by adding specific dose-volume constraints in the interfaces during plan optimization without deteriorating the overall quality of the plan.

IMPROVING THE ARTERIAL INPUT FUNCTION IN DYNAMIC CONTRAST ENHANCED MRI BY FITTING THE SIGNAL IN THE COMPLEX PLANE

C.A.T. van den Berg, F.F.J Simonis, A. Sbrizzi, J.J.W. Lagendijk
Imaging Division, University Medical Centre Utrecht

Introduction: Acquiring an accurate arterial input function (AIF) is essential in dynamic contrast-enhanced (DCE) MRI analysis. Currently two approaches for AIF have been demonstrated in literature; based on magnitude MR data or more recently based on phase MR data. Each method still faces considerable but different technical challenges and robust AIF quantification is still an outstanding problem. Here we demonstrate that fitting the AIF complex data in the complex plane can be used to mitigate noise and bias that arise from solely using phase or magnitude data. The technique is applied to 3T DCE-MRI data of 13 prostate cancer patients.

Methods: DCE-MRI exams were performed on a 3T MR scanner (Achieva, Philips Healthcare using a 3D spoiled GRE (TR/TE 4.0/2 ms flip angle = 8, 120 dyn, 2.4 s temporal resolution). In this IRB approved study 13 patients were included that received also within the same week a DCE-CT exam. In each patient 0.1 mL/kg gadobutrol was injected (1.0 M Gadovist, 1 or 2 mL/s, followed by a saline flush. The femoral arteries were selected for AIF determination. In addition, as a validation a series of test tubes filled with different Gadovist concentrations (0-10 mM) were scanned with the same sequence. The complex AIF signal S was fit to a complex signal model consisting of a magnitude signal model of a steady state, spoiled gradient echo combined with a signal phase model derived from an infinitely long cylinder along B0 with a varying susceptibility. The linear part of the equation was fit separately using the VARPRO method. The derived AIFs from the complex fitting were compared with magnitude only and phase only based AIFs. In addition the DCE-MRI AIFs normalized to given contrast agent dose were compared to the gold standard normalized DCE-CT AIFs.

Results and Discussion: The phantom experiments demonstrated that complex signal fitting leads to very accurate concentration estimates. As the signal model and the enhancement define a spiral-shaped trajectory in the complex plane, the solution space can be confined tremendously improving the robustness to bias and noise. Although the signal is still affected by imperfections such as B0 field drift or inflow, their effects are regularized by the complementary actions of phase and magnitude as they are dependent on different MR signal mechanisms. The in-vivo results indicated that the complex fitting strongly improved the shape of the AIFs, now showing a clear first pass peak, recirculation and a slowly decreasing tail. Magnitude or phase based AIFs demonstrated more unrealistic behaviors. The complex fitting leads to a minimal uncertainty (~ 1 mM) in the concentration estimates over the full dynamic range of the AIF, contrary to the phase and magnitude only methods. The DCE MRI AIFs of the 13 included patients derived from complex signal fitting demonstrated a much higher resemblances to the gold standard DCE-CT AIFs.

Conclusion: By modeling the complex signal from DCE-MRI AIFs can be greatly improved, making it a more stable input for DCE models

ASSESSMENT OF MRI SCANNER GEOMETRIC DISTORTION CORRECTION OPTIONS FOR GYNAECOLOGICAL BRACHYTHERAPY WITH AN IN-HOUSE PHANTOM

Adele Fallows and Jonathan Phillips
Velindre Cancer Centre

Introduction/purpose: Geometric distortion is the displacement of displayed points within an image relative to their true location. Distortion in MR is caused by local imperfections in the magnetic fields, and the effect increases with distance from the isocentre [1].
Brachytherapy dose gradients are 5-10% per mm. Accurate dose calculation depends on precise applicator reconstruction and therefore the spatial accuracy of planning scans. GEC-ESTRO [2] recommends testing the geometric distortion of the MR scanner during commissioning and on-going quality assurance.

Methods/materials: Distortion was examined using an in-house Perspex phantom of water-filled tubes, imaged using a fast-spin echo protocol on a GE Optima MR450w 1.5T scanner. Scans were acquired with and without the '3D geometric correction' option selected. Results were analysed in MATLAB by comparison of the MR rod positions against a 'gold standard' dataset. This allows calculation of the magnitude error: the difference between the 'true' and displayed positions of the rod centre as a function of distance from the isocentre. Initially, a CT dataset was used as the 'gold standard'. The phantom was CT scanned, but an error in the setup necessitated a rescan. The presence of previously unnoticed metallic rings perturbed both the CT and MR images at the centre of the phantom. Some of the rod cross sections in the CT scan displayed as rings, causing difficulty in identifying the centre of these rods.A different approach was adopted, in which a virtual gold standard dataset was constructed from an MR slice acquired at the isocentre, and this was used in the final analysis together with a manual confirmation using a CT slice as the gold standard. The virtual gold standard dataset was validated by comparison with the CT dataset as any imperfections in the construction of the phantom would be visible in the CT set.

Results: Within 150mm of the isocentre, the magnitude error is less than 2mm, and the '3D geometric correction' option had little effect. The magnitude error increases to 4 – 10mm at 200 to 250mm from the isocentre. Using the '3D geometric correction' option reduces the error to less than 6mm over this range.

Conclusions/discussion: Within the range normally required for brachytherapy planning, the geometric distortion is acceptable and little difference is seen if the '3D geometric correction' option is selected, at least within 150 mm of the isocentre. The importance of positioning the MR isocentre close to the brachytherapy applicators has been highlighted. More robust assessment using adaptations of the Wang [3] methodology is being investigated.

References
[1] Quality Control in Magnetic Resonance Imaging. R Lerski, J De Wilde, D Boyce, J Ridgway. IPEM Report 80 (1998).
[2] Recommendations from Gynaecological (GYN) GEC-ESTRO Working Group (IV): Basic principles and parameters for MR imaging with the frame of image based adaptive cervix cancer brachytherapy. JCA Dimopoulos et al. Radiother. Oncol. 103, 113 (2012).
[3] Geometric distortion in clinical MRI systems Part I : evaluation using a 3D phantom. D Wang et al. Magnet. Reson. Imag. 22, 1211 (2004).

IMPACT OF MRI GEOMETRIC DISTORTION ON TANGENTIAL WHOLE BREAST IMRT

Amy Walker[1,2,3], Peter Metcalfe1[2,3], Gary Liney1[2,3,5], Vikneswary Batumalai[2,3,4], Kylie Dundas[1,2,3], Carri Glide-Hurst[8], Geoff Delaney[2,4,6,7], Miriam Boxer2, Mei Ling Yap[2,3,4,6,7], Jason Dowling[9], David Rivest-Henaul[t9], Elise Pogson[1,2.3], Lois Holloway[1,2,3,4,5]

(1) Centre for Medical Radiation Physics, University of Wollongong, Wollongong, NSW, Australia
(2) Liverpool and Macarthur Cancer Therapy Centres, NSW, Australia
(3) Ingham Institute for Applied Medical Research, Liverpool Hospital, Sydney, NSW, Australia
(4) University of New South Wales, Sydney, NSW, Australia
(5) Institute of Medical Physics, School of Physics, University of Sydney, Sydney, NSW, Australia
(6) Collaboration for Cancer Outcomes Research and Evaluation, Liverpool Hospital, Liverpool, NSW, Australia
(7) School of Medicine, University of Western Sydney, Sydney, NSW, Australia
(8) Department of Radiation Oncology, Henry Ford Health System, Detroit, Michigan, USA
(9) Commonwealth Scientific and Industrial Research Organisation Computational Informatics, Australian E-Health Research Centre, Brisbane, Australia

Introduction: There are potential benefits moving from CT-based to MRI-based radiotherapy treatment planning. However, geometric distortion needs to be considered. This study investigates the clinical impact such distortions have on whole breast radiotherapy (WBRT) if left uncorrected. Both phantom and patient measurements were performed to determine if system-related distortion measurements with a phantom can be used to replicate patient distortion measurements.

Methods: CT and MRI datasets for seven WBRT patients were obtained on a wide-bore Philips CT and a wide-bore 3T Siemens Skyra MRI. The CT datasets were retrospectively distorted to match patient geometry as represented on MRI, including both set-up variation and distortions from patient susceptibility. This allows for the determination of the impact of geometric distortion effects alone (without considering additional effects from electron density assignment). Phantom distortion measurements were made on the Siemens Skyra and an open-bore 1T Philips Panorama scanner with matching CT datasets. Deformable registration between the phantom CT and MR images was used to obtain a deformation map of the MRI systems. These phantom-based deformation maps were used to deform each patient CT by the known system distortions. Thus 4 CT datasets were considered per patient i) the original CT, ii) a CT dataset matching the patient geometry on the Skyra, iii) a CT dataset matching phantom distorted geometry on the Skyra and iv) a CT dataset matching phantom distorted geometry on the Panorama. For each dataset, a tangential IMRT treatment plan was generated using a script, with plans individually optimised for each distorted dataset. Plans optimised on the distorted patient geometry were then copied onto the original CT dataset and recomputed, to simulate what would happen if these distorted datasets were used. DVH and visual analysis of these recomputed plans was used to assess whether planning on the geometrically distorted datasets would have resulted in unacceptable plans when treated on the actual patient geometry.

Results: Plans optimised on the CT datasets distorted to the clinical patient MRI showed the greatest variation in DVH criteria when recomputed on the original CT. For datasets distorted to match the patient MRIs incorporating both set-up variation and MRI distortion, 3 of 7 datasets were deemed clinically unacceptable when the distorted plan was recomputed on the original image. One failed the DVH criteria assessment, with the contralateral breast dose too large. The other 2 plans failed on visual assessment, due to patchy dose distribution. Plans optimised on datasets distorted by the phantom measurements on the Skyra and Panorama all passed DVH and visual assessment when recomputed on the original CT with the greatest variation seen from the open-bore system. Mean dose differences in PTV V95% between plans optimised on distorted datasets to those plans recomputed on the original CT datasets were 0.07 ± 1.06% (mean±2), 0.09 ± 2.13% and 0.37 ± 1.45% (Skyra phantom, Skyra patient and Panorama phantom measurements respectively).

Conclusion: No impact on plan dosimetry was seen from either the open-bore or closed-bore MRI systems. Patient results indicate compensating for scanner distortions may improve planning accuracy.

SEGMENTATION OF RADIOTHERAPY TARGET VOLUMES BASED ON MAGNETIC RESONANCE SPECTROSCOPIC IMAGING

Andrea Laruelo, Lotfi Chaari, Jean-Yves Tourneret, Hadj Batatia, Soleakhena Ken, Ben Rowland,
Régis Ferrand and Anne Laprie
Institut Claudius Regaud

Purpose/Objective(s): MR spectroscopic imaging (MRSI) can characterize biochemical, metabolic and pathological changes in brain tissues before they are visible from conventional anatomical images. This makes MRSI a powerful tool to define biologically tailored target volumes for dose escalation in radiotherapy treatments [1,2]. Although the numerous existing quantification techniques, it remains difficult to obtain accurate information from MRSI signals due to biological and experimental conditions decreasing the quality of the data. We present a novel quantification method which alleviates these limitations by exploiting the sparsity of the MRSI data in the wavelet domain in order to increase the signal-to-noise ratio (SNR) of the signals.

Materials/Methods: A set of 20 synthetic brain MRSI grids of size 10x10 were generated based on values commonly reported in the literature [3]. 300 in vivo 3D MRSI voxels from 3 boxes from a healthy volunteer and 2 patients with diagnosed GBM included in the prospective clinical trial Spectro-Glio (NCT01507506) ,were analyzed (1.5T, TE/TR=135ms/1.5s). Metabolic maps were generated by using conventional voxel-by-voxel quantification [4] and the proposed method. This method quantifies simultaneously all the signals within the MRSI box and exploits the sparsity of the MRSI data in the spectral and the spatial dimensions. A Monte Carlo study on synthetic data was performed to compare the robustness of the methods with respect to the noise. To this aim five different levels of white Gaussian noise were added to a synthetic datasets. Estimated metabolite concentrations from in vivo MRSI data were also studied. The agreement between the derived maps and companion MRI images was analyzed. The processing pipeline used for this work has been developed for clinical application in the radiotherapy context as part of the FP7 Marie Curie SUMMER project (Software for the Use of Multi-Modality images in External Radiotherapy). [5]

Results: Results on synthetic data show a significative gain in accuracy and robustness against noise in the results obtained with the proposed method. The errors of the estimated metabolite concentrations are reduced by a mean of 41% (range 24-54% depending on the level of noise). This leads to more accurate metabolite maps for all the levels of noise analyzed in this study. For in vivo data, the spatial distributions of the metabolites are in better accordance with the physiological structures visible from MRI images. In addition, the presented method is able to correctly quantify metabolites that are missed by other methods due to the presence of noise or nuisance components (e.g., lactate). This is especially relevant for the quantification of metabolites present in low concentrations.

Conclusions: Incorporating spectral/spatial information within the quantification model improves significantly the robustness of the process and the accuracy of the resulting metabolite estimates from MRSI data. This leads to better contoured and easy-to–interpret metabolite maps that can be used to define more targeted and more individualized radiotherapy treatments.

References:
[1] Laprie et al IJROBP 2008 [2] Ken et al Rad. Onc. 2013 [3] Safriel et al AJNR 2005 [4]Poullet et al NMR Biomed. 2007 [5]Massoptier et al. Int Symp Biomed Imag 2012

DIRECTLY DERIVE MR ELECTRON DENSITY FOR MR-ONLY RADIATION TREATMENT PLANNING OF BRAIN –AUTOMATED TISSUE SEGMENTATION APPROACH

Huan Yu, PhD, Sunnybrook Research Institute, Sunnybrook Health Sciences Centre
Young Lee, PhD, Medical Physics, Sunnybrook Odette Cancer Centre
Mark Ruschin, PhD, Medical Physics, Sunnybrook Odette Cancer Centre
Irene Karam, M.D., Radiation Oncology, Sunnybrook Odette Cancer Centre
Arjun Sahgal M.D., Associate Professor of Radiation Oncology and Surgery, University of Toronto, Clinician Scientist, Sunnybrook Research Institute, Affiliate Scientist- Toronto Western Research Institute , Radiation Oncology, Sunnybrook Odette Cancer Centre

Introduction and Purpose: MR is the main imaging modality used for target delineation in radiation therapy for the brain. However, it is not usually used on its own due to its lack of electron density (ED). One solution is to assign ED to MR images to generate a pseudo-CT (pCT) image. However, this is difficult because air and bone are not distinguishable from each other in MR images and some tissues have similar MR intensities but large ED differences. In literature, main ED assignment methods include bulk assignment using tissue contours from co-registered CT images, deformable image registration with a population-based Atlas and statistical tissue classification based on MR intensity distribution. These methods are subject to image registration error, variation in patient anatomy and MR intensity variations. This work is aimed at developing a method that can accurately assign tissue ED to generate a pCT using only the information from a patient's MR images.

Methods and Materials: First, a semi-automated tissue segmentation algorithm was developed to differentiate tissues with similar MR intensities and large differences in electron densities. In approximate 12 slices at six levels of head, spatial regions containing sinuses and airways were manually contoured and interpolated in between slices. Then, air, bone, brain, cerebrospinal fluid (CSF), and eyes were automatically segmented using edge detection and anatomical information including location, shape, tissue uniformity and relative intensity distribution. Next, soft tissues - muscle and fat - were segmented based on their relative intensity histogram. Finally, the intensities of voxels in each segmented tissue were mapped into their ED range to generate a pCT by linearly fitting their relative intensity histograms. Co-registered CT was used as a ground truth. 20 stereotactic radiosurgery patients' T1-weighted MR images and CT images were retrospectively acquired for evaluation. The bone segmentations of pCT images were compared with those of CT obtained by using a 300HU threshold. Distances between bone contours were measured automatically by searching for the shortest distances between voxels on the external contours of the skull of pCT and CT. The mean absolute ED (in Hounsfield unit) differences of voxels in each type of tissue segmented were calculated.

Results: The average distance between the contour of the external skull in pCT and the contour in co-registered CT was 0.6±1.1mm (mean±1SD, including registration error). The mean absolute ED differences for bone, brain, CSF, muscle and fat were 78±114 HU, and 21±8 HU, 14±29 HU, 57±37 HU, and 31±63 HU, respectively. The time for manual contouring is about 10 minutes and the average time for automated tissue segmentation and ED mapping is about 5 minutes.

Conclusions and Discussion: The semi-automated MR electron density mapping technique was developed utilizing high soft tissue contrast of MR images and anatomical information to obtain tissue contours without image registration to CT or deformable registration to an Atlas. The generated pseudo-CT is comparable to that of CT in terms of the anatomical position of tissues and similarity of ED assignment. This method can allow MR-only treatment planning.

EVALUATION OF EXTERNAL BEAM RADIOTHERAPY CT-BASED DOSE PLANS RECALCULATED ON MRI-GENERATED DENSITY MAPS

Steffen Hokland[1], Max Köhler[2], Kari Tanderup[3]

(1) Department of Medical Physics, Aarhus University Hospital, Aarhus, Denmark
(2) Philips Healtcare, MR Therapy, Vantaa, Finland
(3) Department of Experimental Clinical Oncology, Aarhus University Hopsital, Aarhus, Denmark

Introduction: Despite the many advantages of MRI over CT the latter continues to be ubiquitous for radiotherapy treatment planning due to the inherent information on radiation attenuation. Electron density maps generated from MRI-images would be needed to omit the CT-scan. We evaluated CT based radiotherapy plans re-calculated on density maps generated using a proprietary algorithm - Magnetic Resonance for Calculating Attenuation (MRCAT)1.

Methods: Nine prostate cancer patients referred for standard radiotherapy received an mDixon-scan (Scanner: Ingenia 1.5T Philips Healthcare, 3D cartesian Fast Field Echo, FOV: 350mm×478mm×300mm, Voxel size: 1.7mm×1.7mm×.25mm, TR=5.7ms, TE1=1.6ms, TE2=3.9ms, Flip angle=10°, Total imaging time=3:14min) in addition to the normal scan protocol. Five-value stratified HU-maps were calculated off-line using the MRCAT algorithm assigning Hounsfield values as either water (42), fat (-106), compact (798) or cancellous bone (160) or finally extra corporeal air (-968). The body outline was cropped to include the union of CT and MRCAT body outlines. Treatment plans (prescribed dose: 78Gy in 39 fractions) were optimised on CT with the requirement that they fulfil local dose constraints (PTV_V90>99%, CTV_V95>99.5%, Rectum_V70Gy<20%, Rectum_V74Gy<1cc). The plans were subsequently re-calculated on the simulated CT images using the monitor units from the original plan. DVH-parameters, PTV_V95, PTV_D98, PTV_Dmean, 2cc_Dmax and Rectum_D2cc, were compared across the two scans. Students's pairwise t-test was used for comparison between MRI and CT based DVH parameters.

Results: In general we recorded higher DVH-parameters for the MRCAT-based calculations. For overall target coverage we found (values listed as 95% confidence interval. p-values are given for a Student's t-test for equality between the two measured values.) PTV_V90(CT)=94.5% [93.6:95.7]%, PTV_V90(MRCAT)=96.3% [95.2:97.4]% (p=0.048) and PTV_D98(CT)=72.3Gy [72.0:72.6]Gy, PTV_D98(MRCAT)=73.3Gy [72.9:73.7]Gy (p=0.003). The original plan was normalised to 100% (78Gy) as PTV mean value. For the corresponding MRCAT PTV_Dmean we found 100.9% [100.7:101.1]% which was significantly greater than 100% with a p-value < 10-5. Rectal dose was also overestimated with MRCAT: D2cc(CT)=73.0Gy [72.7:73.3]Gy and D2cc(MRCAT)=74.1Gy [73.3:74.9]Gy (p=0.008) as well as the global maximum dose to 2cc 80.4Gy [80.3:80.6]Gy (CT) and 81.1Gy [80.9:81:3]Gy (MRCAT).

Discussion: Although significantly greater when compared to the generic plan CT, DVH-parameters calculated on the synthetic CT-scans were comparable with a mean dose overestimation of 0.9% and 1.4% for target mean and minimum dose, respectively. Rectum D2cc was overestimated by 1.5%. The main reason is probably that the current instalment of the MRCAT algorithm renders air filled cavities in the rectum as water. This will yield higher rectal doses and increase the calculated dose the the part of the PTV that encompasses rectum increasing PTV-parameters as well.

1Schadewaldt et al. "Comparison of Dose Calculation On Automatically Generated MR-Based ED Maps and Corresponding Patient CT for Clinical Prostate EBRT Plans", Proceedings AAPM, Austin, Texas, USA, 2014

ACCURACY OF DOSE CALCULATION FOR BRAIN RADIOTHERAPY USING PSEUDO-CTS GENERATED FROM AN UNDERSAMPLED SINGLE ACQUISITION UTE-MDIXON PULSE SEQUENCE

Gisele Castro Pereira, Kuan-Hao Su, Bryan J. Traughber, Melanie S. Traughber, Raymond F. Muzic Jr.
University Hospitals – Case Western Reserve University

Introduction: Previous work[1,2] has demonstrated the technical feasibility of dose calculation using MRI by manual contouring and assigning bulk densities or from various pseudo-CT generation schemes. These prior techniques, although technically feasible, are clinically impractical due to long MR acquisition times and lack of automated workflow. Herein, we used an undersampled single acquisition UTE-mDixon pulse sequence and unsupervised clustering methods to generate a clinically robust workflow for pseudo-CT generation. Dose calculations were then evaluated using a commercial treatment planning system.

Methods/Materials: Five patients were included under a prospective protocol approved by the University Hospitals Case Medical Center Institutional Review Board. Multi-echo MR data (TE = 0.1, 1.5, and 2.8 ms) was acquired using the UTE-mDixon sequence with 25% angular sampling density as previously described by our group[3]. Three image features, Dixon-fat, Dixon-water, and R2*, were used for unsupervised clustering. Five tissue clusters were estimated using the fuzzy c-means algorithm (FCM). Pseudo-CTs were generated by a voxel-wise linear combination of the membership functions of the FCM. All patients also had a reference CT for attenuation correction. Four data sets were generated for each patient and used for dose calculation: 1) the reference CT; 2) the pseudo-CT created from UTE-mDixon and unsupervised clustering; 3) a T2 image for manual contouring and bulk density assignment; and 4) the same reference CT image but with a homogenous density assignment. Both 3D and volumetric modulated arc therapy plans were generated for each image set using a Pinnacle Planning System with the Collapsed Cone Convolution algorithm. A treatment plan was created using the reference CT (i.e., reference approach). This plan was then transferred onto the three other methods and the dose was recalculated by keeping the same field parameters and monitor units. Dose point calculation and gamma index with criteria of 3%/3mm were used to evaluate the dose accuracy.

Results: The combined MR acquisition and pseudo-CT generation time was approximately four minutes. The point dose calculation agreement is excellent for the pseudo-CT and bulk density methods with very minimal difference compared to the reference CT. The average percentage dose differences from the CT were 0.7, 0.5 and 3.3%, and the average percentages of points passing the gamma index were 97.1, 96.3 and 89.6% for the pseudo-CT, bulk density and homogenous approaches, respectively.

Conclusions: A major limitation of prior work was impractical MR scanning, often over ten minutes[4,5], which frequently included multiple pulse sequences and acquisitions. The method described here, is a single acquisition UTE-mDixon, which provides sufficient data for pseudo-CT generation and the data quality was adequate for accurate treatment planning dose calculation with a commercial system. Importantly, the workflow was nearly automated and the combined MR acquisition and pseudo-CT generation time was only four minutes, thus providing a practical approach for translation of MR based therapy planning to the clinic.

References: 1Berker, Y. et al. MRI-based attenuation correction for hybrid PET/MRI systems: a 4-class tissue segmentation technique using a combined ultrashort-echo-time/Dixon MRI sequence. Journal of nuclear medicine : official publication, Society of Nuclear Medicine 53, 796-804, doi:10.2967/jnumed.111.092577 (2012). 2 Stanescu, T., Jans, H. S., Pervez, N., Stavrev, P. & Fallone, B. G. A study on the magnetic resonance imaging (MRI)-based radiation treatment planning of intracranial lesions. Physics in medicine and biology 53, 3579-3593, doi:10.1088/0031-9155/53/13/013 (2008). 3 Hu, L. et al. k-space sampling optimization for ultrashort TE imaging of cortical bone: applications in radiation therapy planning and MR-based PET attenuation correction. Med Phys 41, 102301, doi:10.1118/1.4894709 (2014). 4 Jonsson, J. H., Johansson, A., Soderstrom, K., Asklund, T. & Nyholm, T. Treatment planning of intracranial targets on MRI derived substitute CT data. Radiother Oncol 108, 118-122, doi:10.1016/j.radonc.2013.04.028 (2013). 5 Hsu, S. H., Cao, Y., Huang, K., Feng, M. & Balter, J. M. Investigation of a method for generating synthetic CT models from MRI scans of the head and neck for radiation therapy. Physics in medicine and biology 58, 8419-8435, doi:10.1088/0031-9155/58/23/8419 (2013).

USE OF IMAGE CO-REGISTRATION TO INTEGRATE DIAGNOSTIC MRI INTO THE RADIOTHERAPY PLANNING PROCESS FOR HEAD AND NECK CANCER

Richard Speight, Robert Chuter, Jonathan Sykes, Andrew Scarsbrook, Mark Gooding, Aymeric Larrue and Robin Prestwich
Leeds Cancer Centre

Purpose: There has been considerable recent interest in the use of MRI to improve the accuracy of delineation of gross target volumes (GTV) and organs at risk (OAR) for head and neck squamous cell carcinoma (HNSCC). The gold standard (GS) delineation is considered to be delineation on treatment position MRI (MRI-RT) rigidly registered to a planning CT (pCT); however MRI-RT is not widely available. This study aimed to assess whether optimising image registration of a diagnostic position MRI (MRI-D) to pCT is superior to delineation on pCT alone or is an adequate surrogate for MRI-RT.

Method: Five HNSCC patients underwent contrast-enhanced CT and T1 weighted gadolinium-enhanced MRI both in (MRI-RT) and out of (MRI-D) an immobilisation mask during a prospective imaging study. A Radiation Oncologist delineated GTV and OARs on CT, MRI-RT and MRI-D on 3 separate occasions. Consensus contours from the 3 delineations were produced using majority vote. GS structures were defined as consensus contours from MRI-RT transposed to CT using rigid registration. The GS was compared to consensus contours produced by 6 other methods: MRI-D transposed to CT with deformable image registration (DIR) of the whole imaging field; MRI-D transposed to CT with either rigid registration or DIR optimised on a 3cm ROI around the GTV; MRI-D transposed to CT with either rigid registration or DIR optimised on a 3cm ROI around the brainstem (as a proof of principle for a single OAR); and CT alone delineations. All registrations were performed using Mirada RTx v1.4 (Mirada Medical, Oxford UK) and 8 contour comparison metrics (only DICE quoted here) were calculated with ImSimQA v3.1.5 (OSL, Shrewsbury UK) to assess intra-observer variability and comparison of GS structures to the 6 test methods.

Results: Contouring on MRI-RT or MRI-D reduced intra-observer variability compared to CT (DICE mean ranges 0.76-0.99 for MRI and 0.39-0.84 for CT). GTV and OAR delineation consistency with the GS improved with the use of MRI-D compared to CT alone contouring. Highest concordance with the MRI-RT GS was obtained when DIR was used over the whole imaging field or rigid registration was used in a region around the anatomy of interest. For example, brainstem mean DICE was 0.75 and 0.82 for MRI-D contours transposed with DIR over the whole patient and rigid registration in the ROI respectively, compared to 0.68 for pCT alone contouring. Using DIR in the ROI was found to reduce concordance (eg brainstem mean DICE result dropped to 0.22).

Conclusions: Intra-observer reproducibility of contouring with MRI was found to be superior to that with CT, indicating that the addition of MRI to the workflow for HNSCC radiotherapy planning is desirable. This study demonstrates that in the absence of access to dedicated MRI-RT, image registration software can facilitate integration of MRI-D into the treatment pathway with a benefit in accuracy for GTV and OAR delineation. MRI-D is most appropriately used when contours are transposed to pCT with DIR over the whole imaging field or with rigid registration based on a region around the anatomy of interest.

INVESTIGATION OF MR FIELD HOMOGENEITY FOR AN MR-GUIDED RADIOTHERAPY SYSTEM WITH AN MR-ON-RAILS SCANNER

T. Stanescu, J. Liu, M. Drangova, D. Jaffray
Princess Margaret Cancer Centre, UHN & Radiation Oncology, University of Toronto

Purpose: An MR-guided radiotherapy facility consisting of three rooms dedicated for brachytherapy, MR simulation and external beam activities is available at our institution. The 1.5T MR scanner is mounted on ceiling rails via a mover assembly and can travel to perform imaging in all rooms. For specific scenarios, the MR movement implies translations and 180° rotations which can potentially modify the magnetic field profile of the environment due to MR's coupling with ferromagnetic materials in functional components (linac, brachy/linac table) and infrastructure (support beams, door frames). The aim of the study was to investigate the MR magnet shimming and characterize the field homogeneity for all envisioned clinical scenarios.

Methods: The MR has several levels of shimming: a) passive (iron plates), b) active preset via service tune-up, and c) active 3D shim or patient-specific. The linear inhomogeneities are compensated by applying offset currents to the gradient coils whereas the second order corrections are addressed by adjusting currents on five shim coils which are integrated into the gradient coil. Each MR imaging position/room has a dedicated optimal shim setting. Specific methods were used to quantify and monitor the MR shimming: i) measurement of the water spectral peak, ii) manufacturer's service shim tune-up procedures (Phantom Shim, Phantom Shim Check), and iii) B0 mapping technique. The field homogeneity metrics were the FWHM for i), the root mean square (Brms) and peak-to-peak (Bpp) field values as determined from phase image data acquired on a QA spherical phantom with uniform signal. The B0 mapping technique was based on acquiring phantom scans with a double-echo GRE sequence and image post-processing. Measurements were performed for multiple clinical scenarios: in the MR Simulation room (home position), in the brachytherapy suite with the MR diagnostic table, inside the linac vault at pelvis/head-and-neck imaging position with the MR service end oriented towards the linac. Experiments were also conducted to investigate the MR shim effects related to the history of the MR movement in the facility, e.g. quantify MR shim in the MR Simulation room after the MR was in the linac/brachytherapy room.

Results and Discussion: The manufacturer's established values for an optimal shim are 0.4 ppm and 3 ppm for Brms and Bpp, respectively, as per service reports from method ii). The B0 mapping procedure was tailored to closely match the results from method ii) for a wide range of shim settings, e.g. GRE double-echo sequence parameters. FWHM values showed variations from the baseline when the shim was quantified in the MR Sim room after imaging in the linac vault (e.g. pelvis position). The fluctuations tend to cancel out when the MR is moved in the opposite direction, in the brachytherapy room. This is assumed to be caused by transient effects generated by currents induced in the MR system and magnetic field priming of the imaging environment. Overall, the observed fluctuations did not impact significantly the Brms and Bpp values.

Conclusion: The field homogeneity was found to be within the manufacturer specifications for all identified clinical uses of the MR scanner.

AUTOMATED BONE SEGMENTATION TO SUPPORT SYNTHETIC CT IN THE PELVIS

Lianli Liu, James Balter, Yue Cao, Shruti Jolly, Jeffrey Fessler
The University of Michigan

Introduction: While ultrashort TE imaging techniques have the capacity to roughly separate air and bone, the mobility of air in the pelvis limits their use for synthetic CT classification methods that include other forms of contrast (e.g. T2-weighted imaging). In support of multispectral synthetic CT in the pelvis, a bone identification scheme was developed to eliminate regions where air may be present and support combined classification of voxels that may contain some bone along with other (fluid, fat, solid tissue) tissues/materials.

Methods: A shape atlas was developed to support pelvis bone identification. A retrospective protocol was approved to collect CT image volumes for 12 female patients who underwent radiotherapy to the pelvis. In addition, 8 subjects participated in a prospective IRB-approved protocol in which they underwent both CT simulation as well as MRI to investigate optimization of MR imaging for radiotherapy. Bones were extracted from CT by intensity thresholding and editing to cut off the femoral heads and spine. The shape atlas was constructed by deformably aligning the population of segmented pelvic bone images using an intensity-based multiresolution B-spline approach. Principle component analysis (PCA) was applied to the B-spline coefficients. An alignment cost function based on the mean squared difference between the deformed atlas and target MRI volumes was applied. The search space of eigenvalues across the first 3 eigenvectors was mapped and demonstrated to be smooth, permitting an efficient search for the optimal bone shape over a limited search range. To improve sensitivity to bone locations, a dilation of the optimal mask shape was investigated for its ability to maintain sufficient specificity in rejecting air voxels.

Results: Using the first eigenmode only, the percentage of correctly identified bone voxels was 84% as compared to 86% when fitting the model to the source CT images by maximizing the percentage of identified bone voxels. Including the second and third eigenmodes to the model resulted in an improvement of less than 2%. Dilating the bone-containing space by 5mm improved the overlap with true bone to 96%, while the percentage of air voxels mislabeled as bone remained below 0.6%.

Summary: A shape atlas is a feasible method for separating bone from air to aid synthetic CT generation in the pelvis using multiple image contrasts.

Supported by NIHR01EB016079